nature

https://doi.org/10.1038/s41586-025-08873-8

Accelerated Article Preview

Structures and mechanism of human mitochondrial pyruvate carrier

Received: 10 April 2024

Accepted: 6 March 2025

Accelerated Article Preview

Cite this article as: Liang, J. et al. Structures and mechanism of human mitochondrial pyruvate carrier. *Nature* https://doi.org/10.1038/s41586-025-08873-8 (2025)

Jiaming Liang, Junhui Shi, Ailong Song, Meihua Lu, Kairan Zhang, Meng Xu, Gaoxingyu Huang, Peilong Lu, Xudong Wu & Dan Ma

Structures and mechanism of human mitochondrial pyruvate carrier

Jiaming Liang[1, 2, 3, 4#], Junhui Shi[1, 2, 3, 4#], Ailong Song[1, 2, 3, 4#], Meihua Lu[2, 3, 4], Kairan Zhang[2, 3, 4], Meng Xu[1, 2, 3, 4], Gaoxingyu Huang[2, 3, 4], Peilong Lu[2, 3, 4], Xudong Wu[2, 3, 4*] and Dan Ma[2, 3, 4*]

1. Fudan University, Shanghai, China
2. Key Laboratory of Structural Biology of Zhejiang Province, School of Life Sciences, Westlake University, Hangzhou, Zhejiang, China.
3. Westlake Laboratory of Life Sciences and Biomedicine, Hangzhou, Zhejiang, China.
4. Institute of Biology, Westlake Institute for Advanced Study, Hangzhou, Zhejiang, China.

# These authors contributed equally: Jiaming Liang, Junhui Shi, Ailong Song.

* Corresponding emails: D. Ma madan@westlake.edu.cn, X. Wu wuxudong@westlake.edu.cn

Key Words: mitochondrial pyruvate carrier; MPC; pyruvate metabolism; transporter; cryo-EM structure; mitochondria; drug target; pyruvate; UK5099.

Summary

Mitochondrial pyruvate carrier (MPC) is a mitochondrial inner membrane protein complex essential for uptake of pyruvate into matrix as the primary carbon source for tricarboxylic acid (TCA) cycle[1,2]. Here, we report six cryo-EM structures of human MPC in three different states: three structures obtained at different conditions in intermembrane space (IMS)-open state with highest resolution of 3.2 Å, a structure of pyruvate-treated MPC in occluded state at 3.7 Å, and two structures in matrix-facing state bound with the inhibitor UK5099 or an inhibitory nanobody on the matrix side at 3.2 Å and 3.0 Å, respectively. MPC is assigned into a heterodimer consisting of MPC1 and MPC2, with the transmembrane domain adopting pseudo-C2-symmetry. Approximate rigid body movements occur between the IMS-open state and the occluded state, while structural changes primarily on the matrix side facilitate the transition between the occluded state and the matrix-facing state, revealing the alternating access mechanism during pyruvate transport. In the UK5099-bound structure, the inhibitor fits well and interacts extensively with a pocket that opens to the matrix side. Our findings provide important insights into the mechanisms underlying MPC-mediated substrate transport, and the recognition and inhibition by UK5099, which will facilitate future drug development targeting MPC.

Introduction

MPC transports pyruvate, a crucial metabolite mainly derived from glycolysis, from cytosol into mitochondrial matrix. Within the matrix, pyruvate serves as the primary carbon source for TCA cycle, supporting the generation of ATP and providing substrates for various biosynthetic processes[3]. Occupying the central node for cell metabolism, MPC-mediated pyruvate uptake connects multiple key metabolic pathways including those for carbohydrates, amino acids and fatty acids[4].

MPC is composed of two paralogous subunits, mainly MPC1 and MPC2 in higher eukaryotes. In addition to these two subunits, an alternative subunit called MPC3, which can functionally replace MPC2, has been identified in yeast[1,2]. Besides, a homologous subunit

functionally equivalent to MPC1 was reported to uniquely expressed in postmeiotic male germ cells of placental mammals and named MPC1L[5]. MPC subunits exhibit significant sequence homology to each other and are conserved across different species. Notably, there are topology similarities predicted between MPC and SemiSWEET sugar transporters [4,6].

Environmental pH plays a critical role in substrate transport mediated by MPC[7,8], and conversely, MPC activity can also impact the pH of its surrounding environment[9,10]. The pH difference between the mitochondrial intermembrane space (IMS, weakly acidic) and the matrix (weakly alkaline)[11] is important for pyruvate transport by MPC. In turn, malfunction of MPC may result in intracellular and extracellular acidification due to the accumulation of lactic acid, a byproduct of increased glycolytic flux. This phenomenon is often observed in tumor microenvironment, where cancer cells exhibit heightened glucose consumption and lactate production, known as the Warburg effect[12,13].

Since identification and characterization, MPC has sparked significant interest due to the importance in cellular metabolism and its association with various human diseases, including cancers[14-16], heart failure[17,18], and neurodegeneration[19-21]. Dysfunction of MPC has also been implicated in metabolic disorders and impaired energy metabolism[22,23]. More and more studies suggest MPC as a promising therapeutic target for the treatment of metabolically dependent cancers like androgen receptor (AR)-driven prostate cancer, metabolic disorders including type-2 diabetes, neurodegenerative diseases, and severe COVID-19[24].

Despite the importance of MPC, its three-dimensional structures are lacking and molecular mechanism for substrate transport remains unelucidated. Here, we report six cryo-EM structures of human MPC: three IMS-open structures best at 3.2 Å resolution, an occluded structure of pyruvate-treated MPC at 3.7 Å resolution, a matrix-facing structure with the transport path blocked by a nanobody at 3.0 Å resolution, and a 3.2 Å-resolution structure bound with UK5099, a well-known cyanocinnamate-based MPC inhibitor that suppresses tumor growth[7,14,25,26]. Our study reveals the structural assignment of MPC, molecular mechanism of substrate transport, as well as recognition and inhibition mechanism by the

inhibitor UK5099, which will facilitate drug development for the treatment of metabolically dependent cancers and other related human diseases.

Results

Structures of MPC in an IMS-open state

Human MPC1 and MPC2 were recombinantly co-expressed in Expi293F cells before the complex was purified into homogeneity. Proteoliposome-based transport assay results suggested that wild-type (WT) MPC could actively transport pyruvate (Extended Data Fig. 1a-c). To increase the size of the MPC complexes to facilitate cryo-EM studies, we performed nanobody (Nb) screening and finally selected two Nbs (Nb1 and Nb2) targeting MPC. Transport assay results suggested that Nb1 binding did not affect MPC transport activity, whereas Nb2 binding inhibited substrate transport (Extended Data Fig. 1d). We generated different MPC-Nb complexes with or without the supplementation of pyruvate or UK5099 (Extended Data Fig. 1e) for cryo-EM analysis (Extended Data Figs. 2, 3 and Extended Data Table 1). Uncropped gels for gels in Extended Data Fig. 1e and those in following Extended Data Figures, see Supplementary Fig. 1.

Since pyruvate transport by MPC exhibits pH dependency[7], to obtain MPC structures in different conformations, we prepared cryo-EM samples of MPC-Nb complexes with or without pyruvate treatment at different pH values. pH 8.0 was used to mimic the matrix side condition and pH 6.8 was used to mimic the IMS side condition. We obtained cryo-EM maps for apo MPC-Nb1 complex purified at pH 8.0 and pH 6.8, and for pyruvate-treated MPC in complex with Nb1 purified at pH 8.0, at resolution of 3.2 Å, 3.4 Å and 3.4 Å, respectively (Extended Data Fig. 2). The MPC structures built based on these maps are almost identical and exhibit an IMS-open conformation (Fig. 1a, b and Extended Data Fig. 4a, b). Consistent with previous topology studies on MPC[27], both MPC1 and MPC2 consist of three transmembrane helices, with their N-termini located on the matrix side and C-termini located on the IMS side, respectively. Notably, in MPC2, there is an amphipathic helix (APH) at the N-terminus, which serves as the major epitope region for Nb1. This may explain why density for MPC2-APH is

clearly visible, while density for a similar N-terminal region of MPC1 is too weak for model building in all the cryo-EM maps. The transmembrane domain (TMD) of each subunit is arranged into a 1-3-2 triple-helix bundle (THB), similar to the helix arrangement in SemiSWEETs[28-30]. Superimposition of TMDs of MPC1 and MPC2 indicates a significant structural similarity (Extended Data Fig. 4c), and therefore, TMD of MPC is assigned into pseudo-C2-symmetry along the axis perpendicular to the membrane.

APH in MPC2 may be able to interact with mitochondrial inner membrane and embed into the lipid bilayer, which is facilitated by hydrophobic residues in APH that face to the membrane (Extended Data Fig. 4d). Additionally, the multiple positively charged N-terminal residues may interact with the negatively charged phosphate groups of the membrane lipids (Extended Data Fig. 4d). Interestingly, we identified a lipid molecule cardiolipin, which is abundant in mitochondrial inner membrane, lies between the MPC2-APH and MPC1-TMD (Fig. 1b and Extended Data Fig. 4e).

Electrostatic analysis reveals that the regions exposed to IMS and matrix are highly charged, and a cut-away surface illustration indicates MPC is open towards IMS (Fig. 1c). We found a large side cleft that accommodates a phosphatidylcholine (PC) (Fig. 1a-c and Extended Data Fig. 4f). The lipid mediates indirect interaction between MPC1 and MPC2 by connecting the cleft-forming transmembrane helices including MPC1-TM1 and MPC2-TM2 (Fig. 1b). The observation of lipids in the structure seems to be consistent with previous studies about the possible correlation between lipid composition of mitochondrial membrane and MPC activity[31]. In addition to the indirect interactions mediated by the lipid, there are extensive direct inter-subunit interactions on the matrix side, particularly around the putative transport path (Fig. 1d). These interactions involve a hydrophobic interaction network formed by residues Phe69, Val73 and Leu80 in MPC1, as well as Phe42, Trp82, Tyr85, Ile89 and Leu96 in MPC2. Furthermore, a hydrogen bond is formed between Asn77 in MPC1 and Tyr85 in MPC2. These interactions not only contribute to the heterodimer formation but also play a role in maintaining the closed conformation on the matrix side.

Structure of MPC in an occluded state

In contrast to structures of apo MPC-Nb1 at pH 6.8 and pyruvate-treated MPC-Nb1 at pH 8.0, which exhibit IMS-open conformation (Extended Data Figs. 2b, c and 4a, b), we were able to obtain a structure of MPC that adopts a different conformation with the sample of pyruvate-treated MPC-Nb1 at pH 6.8 (Fig.2 a, b and Extended Data Fig. 3a). We found a cardiolipin lies between MPC1-TMD and MPC2-APH (Fig. 2b), similar to that in the IMS-open structure (Fig. 1b), indicating that this lipid may be a constitutive component of the MPC complex. A cut-away surface illustration shows that transport path of MPC is closed on both the IMS and matrix sides (Fig. 2c), suggesting that this structure represents an occluded state during substrate transport. These results indicated that the occluded state may be induced by the pyruvate treatment at pH 6.8. It is challenging to clearly identify bound pyruvate in the 3.7 Å MPC structure. Nevertheless, a small but highly positively charged pocket emerges within the putative transport path (Fig. 2c), formed by highly conserved residues from both MPC protomers including Asn33, Tyr62, Phe66, His84 in MPC1 and Lys49, Trp82, Asn100 in MPC2 (Fig. 2d and Extended Data Fig. 5a), which may correspond to the pyruvate substrate binding site. Transport assay results demonstrated that mutating the putative pyruvate binding site residues MPC2-Lys49, Trp82, and Asn100 to alanine significantly decreased pyruvate transport (Fig. 2e and Extended Data Fig. 5b-d), underscoring the critical role of these residues in substrate transport.

On the IMS side of this occluded structure, the loops between TM1 and TM2 (L1 loops) from both subunits approach to each other and generate 'zipper'-like interactions (Fig. 2f and Extended Data Fig. 5e). Specifically, a salt bridge is formed between MPC1-Glu49 and MPC2-Lys66 at the center of the loops. Hydrogen bonds are formed between MPC1-Asp43 and MPC2-Ser68 at one end of the L1 loops, and between MPC1-Ser52 and MPC2-Asp59 at the other end. Interactions between the 'zipper' forming residues tighten surrounding structural elements towards the central transport path, resulting in a closed conformation on the IMS

side. Furthermore, Arg54 in TM2 of MPC1 interacts with MPC2-Asp59 through electrostatic interaction, which may further stabilize interactions between the L1 loops (Fig. 2f). To examine the importance of residues on the L1 loops, we mutated corresponding residues to alanine (Extended Data Fig. 5b) and performed transport assay. MPC complexes carrying either MPC1-S52A or MPC2-K66A mutation exhibited significantly lower transport activity compared to WT MPC (Fig. 2g and Extended Data Fig. 5f), indicating that the interactions between the L1 loops are important to substrate transport.

Below the L1 loops on the IMS side, we observed that polar residues including Thr56 and Gln91 in MPC1, and Gln71, Ser72 and Gln110 in MPC2 mediate the interaction between MPC1 and MPC2 through hydrogen bonds (Fig. 2h and Extended Data Fig. 5g). We mutated either Gln71 or Gln110 in MPC2 to alanine to examined pyruvate uptake (Extended Data Fig. 5b). Strikingly, both mutations decreased pyruvate transport of MPC by more than 90% (Fig. 2i and Extended Data Fig. 5h). We speculate that these residues may be important for the interactions between MPC1 and MPC2 to maintain the occluded conformation on the IMS side, and therefore crucial for substrate transport. The residue corresponding to Gln110 in human MPC2 is conserved in yeast MPC2 but substituted by a histidine residue in yeast MPC3, and yeast MPC1/MPC3 complex exhibits higher substrate transport activity compared to yeast MPC1/MPC2 complex[27]. We mutated human MPC2-Gln110 to histidine (Extended Data Fig. 5b) and examined the effect on MPC activity and found that the mutated complex can efficiently transport pyruvate with higher activity compared to WT human MPC (Fig. 2i and Extended Data Fig. 5h), which is consistent with previous studies.

Structure of UK5099-bound MPC

UK5099 is a well-established inhibitor of MPC[7,26,32,33] and is frequently used in functional studies of MPC and studies towards MPC-related diseases [25,32,34,35]. However, the precise mechanism of inhibition by UK5099 is still unclear. To investigate the recognition and inhibition mechanism of UK5099, we treated the MPC-Nb1 complex with UK5099 for cryo-EM analysis. We obtained a cryo-EM map at 3.2 Å resolution (Fig. 3a and Extended Data Fig.3b), enabling

us to build a structural model and identify the density corresponding to UK5099 and its binding site (Extended Data Fig. 6a, b).

In the structure of the UK5099-bound MPC-Nb1 complex, UK5099 inserts from the matrix side of MPC to the position of the putative pyruvate binding pocket in the occluded state (Fig. 3b). As a result, the pyruvate transport path is blocked by UK5099. Extensive polar interactions and hydrophobic interactions are found between UK5099 and MPC (Fig. 3c and Extended Data Fig. 6b). The carboxyl group of UK5099 inserts deeply into the binding pocket and forms hydrogen bonds with Asn33, Tyr62 and His84 in MPC1, as well as a salt bridge with Lys49 in MPC2. The cyano group of UK5099 forms a hydrogen bond with Asn100 in MPC2, and the 1-phenylindole group of UK5099 is engaged in hydrophobic interactions with residues including Phe66, Phe69, Leu80 in MPC1 and Trp82, Tyr85, Leu96 in MPC2. (Fig. 3c). It is noteworthy that all residues forming the putative pyruvate binding pocket in the occluded structure also participate in UK5099 binding (Figs. 2d, 3c). This structure suggests that UK5099 directly binds to the pocket on the matrix side of MPC and inhibits substrate transport by blocking the transport path.

To validate the UK5099 binding pocket, we compared the relative binding capabilities of mutants carrying K49A, W82A, W82D or N100A mutations in MPC2 to WT, and found that binding to UK5099 was dramatically weakened in all these mutants (Extended Data Fig. 6d). Among these mutants, only the MPC2-W82D mutant exhibited similar level of pyruvate uptake in 30 s compared to WT (Figs. 2e, 3d and Extended Data Fig. 6e). We determined the IC_{50} values of UK5099 inhibition for substrate transport by both the WT MPC and the mutant carrying the MPC2-W82D mutation. The IC_{50} value of the mutant was more than 300-fold higher than that of the WT MPC (Fig. 3e). These results suggested that the inhibition efficiency of UK5099 is significantly lower for the UK5099 binding pocket mutant. The findings highlight the critical role of corresponding residues in the binding and inhibition of MPC by UK5099.

We also performed ligand docking with UK5099 and other known MPC inhibitors towards MPC[36,37]. The results indicated that the top model, which had the lowest binding energy during

calculation, of each tested inhibitor exhibited a similar binding mode to that of UK5099 in the cryo-EM structure (Extended Data Fig 6.f, g). To be more specific, all inhibitors tend to insert at least three closely arranged polar atoms deeply into the pocket as UK5099 does, forming extensive hydrogen bonds with UK5099-interacting residues in MPC (Fig. 3c). Besides, the inhibitors orient their hydrophobic moieties towards the sub-pocket surrounded by multiple hydrophobic residues similar to UK5099 (Fig. 3c and Extended Data Fig. 6f, g). Above analyses are consistent with previous studies about MPC inhibitors development[36,37], and provide a reasonable explanation for why many different classes of highly potent MPC inhibitors share common features of closely arranged hydrogen bond-forming groups connected to an aromatic ring structure.

MPC Structure in a matrix-facing state

To capture MPC structure in other possible states and achieve higher resolution, we introduced Nb2 that was compatible with Nb1 to the pyruvate-treated MPC in addition to Nb1 at pH 6.8 and obtained a cryo-EM map for Nb1-MPC-Nb2 tertiary complex with a resolution of 3.0 Å (Fig. 4a and Extended Data Fig. 3c).

In this structure, Nb2 binds to MPC on the matrix side and inserts into the transport path with a short connecting loop of a beta hairpin (Fig. 4b). MPC adopts a matrix-facing conformation (Fig. 4c). Similar to UK5099 (Fig. 3c), Nb2 interacts with residues along the transport path by forming a hydrogen bond between the carboxyl group of Nb2-Glu105 and side chain of MPC1-Tyr62, a salt bridge between Nb2-Glu105 and MPC2-Lys49, as well as hydrophobic interactions between the hydrophobic portion of the Nb2-hairpin and MPC1-Phe66/Phe69/Leu80, MPC2-Trp82/Tyr85/Leu96. In addition, Nb2 also forms hydrogen bonds with MPC2-Tyr85 and some other residues in MPC loops on the matrix side (Fig. 4d).

Through structural superimposition, we found that the structure of TMDs in the Nb2-bound and UK5099-bound MPC complexes are highly similar, and only minor structural differences could be observed for residues along the transport path that form corresponding pockets to accommodate Nb2 and UK5099 (Fig. 4e). These results suggest that the two inhibitor-bound

structures may represent a pre-existing matrix-facing conformation in the substrate transport cycle of MPC. This conformation appears to be stabilized rather than induced by UK5099 and Nb2, as it is unlikely that two distinct inhibitory molecules would induce the same matrix-facing state. We compared the binding patterns of MPC with the two inhibitory molecules and found that the polar interactions between the carboxylate groups of UK5099 and Nb2 and the putative pyruvate binding pocket residues, MPC1-Tyr62 and MPC2-Lys49, are similar (Fig. 4f). We speculate that the carboxylate group of pyruvate may also form similar interactions with these residues during binding.

MPC structural changes during transport

Comparing structure of MPC-TMD in the occluded state with that in the IMS-open state reveals dramatic conformational changes. TMDs of MPC1 and MPC2 rotate towards each other on the IMS side to accomplish the state transition (Fig. 5a). However, intra-subunit structural arrangements remain largely unchanged with only minor structural differences in TM1 of both MPC1 and MPC2 (Fig. 5b). These structural observations support that approximate rigid body movements happen during substrate transport to accomplish the transition between IMS-open state and occluded state. The approach of the L1 loops from both subunits lead to the closure of the substrate transport path on the IMS side in the occluded state (Fig. 2b, f). The movements of MPC1-TM1 and MPC2-TM2 narrows the hydrophobic side cleft that accommodates the PC molecule in the IMS-open structure (Fig. 1b), and we could not find density for PC between MPC1-TM1 and MPC2-TM2 in the map of MPC in the occluded state.

Structural alignment between MPC TMDs in occluded state and matrix-facing state (Nb2-bound) suggested that the structural differences between these two structures are mainly observed on the matrix side (Fig. 5c). The matrix-facing conformation and the resulting opening on the matrix side are primarily generated through structural changes at the matrix side of the helical bundle, which swings toward the peripheral regions (Fig. 5c, d and Extended Data Fig. 7). We speculate that the residues adopting conformational changes at the matrix

end of the transport path may serve as the gating residues and control the open or closure of substrate transport path on the matrix side.

The structures of MPC in IMS-open, occluded and matrix-facing states reveal the alternating access mechanism for pyruvate transport. The putative pyruvate binding site is alternatively exposed to the IMS side and matrix side in the IMS-open and matrix-facing states, while it is fully closed in the occluded state (Fig. 5e). Notable differences are observed in the configurations of the conserved MPC2-Lys49, which may directly interact with pyruvate (Fig. 5e). These structural features enable pyruvate to access the binding site during the IMS-open state, triggering conformational changes into the occluded state, and subsequently reaching the matrix-facing state for substrate release into the matrix.

Discussion

Our structural and functional analyses of MPC provide important insights into the molecular mechanism of pyruvate transport and the inhibition mechanism by UK5099. We obtained cryo-EM structures of MPC in three distinct states: IMS-open, occluded, and matrix-facing. These structures reveal the alternating access mechanism of MPC during substrate transport. Notably, the transition between the IMS-open state and the occluded state involves approximate rigid-body movements between the two subunits, resulting in significant structural changes (Fig. 5a, b). In contrast, the transition between the occluded and the matrix-facing state involves minor structural differences, with the helical bundle slightly open on the matrix side in the matrix-facing state, while the remainder of the structure remains largely unchanged, particularly on the IMS side (Fig. 5c). The rearrangements of several hydrophobic residues on the matrix side open the transport path (Fig. 5d) and generate a pocket in the matrix-facing state, which allows the binding of UK5099 and subsequent inhibition. UK5099 may reach the binding site through passive diffusion across mitochondrial membranes or translocation by MPC as implied by previous studies[7,26,38], since the IMS-open MPC bears a large opening that may allow UK5099 to directly gain access to the binding site. Some more hydrophobic keto-

acids, such as phenylpyruvate and alpha-ketoisocaproate that can inhibit pyruvate transport[26], may also get stuck in the same pocket on the matrix side.

In the two matrix-facing structures, both UK5099 and Nb2 insert a carboxyl group into the transport path, generating polar interactions with MPC1-Tyr62 and MPC2-Lys49. The hydrophobic portion of these inhibitors are stabilized by hydrophobic residues within the binding pocket (Fig. 3c and 4d). Given that pyruvate and other reported substrates of MPC[26] all contain a carboxyl group, it is plausible that these substrates share a similar binding mode with the MPC. However, slight conformational rearrangements of the side chains of putative ligand-binding pocket residues may be necessary to accommodate the transport of substrates with varying sizes. Corroborating above hypothesis, the putative substrate binding site, fully encapsulated in the occluded state, becomes accessible from the IMS side in the IMS-open state and from the matrix side in the matrix-facing state (Fig. 5e).

MPC subunits are conserved in primary sequences among different species (Extended Data Fig. 8a, b), and sequence alignment results also suggest that residues in L1 loops and along transport path are highly conserved, indicating that MPC from different species may adopt a similar mechanism for pyruvate transport. It worth noticing that the UK5099 binding pocket forming residues of MPC1-Phe69 and MPC2-Tyr85 in human are replaced by Tyr and Trp in yeast, respectively. We generated corresponding mutations based on our cryo-EM structure model of UK5099-bound MPC and found that these substitutions narrow the opening of the pocket on the matrix side (Extended Data Fig. 8c), which may require UK5099 to overcome higher energy barrier to enter the pocket from the matrix side. This finding is consistent with previous studies showing that yeast MPC exhibits a much lower affinity for UK5099 compared to mammalian MPC[8].

MPC structures in this study are compared to previously reported crystal structures of bacterial SemiSWEETs[28-30]. We found the structure of MPC in IMS-open state closely resembles an inward-open (cytoplasm-facing) structure of a SemiSWEET (Extended Data Fig. 9a), the MPC structure in occluded state shows significant similarity to the SemiSWEETs

structures in occluded conformation (Extended Data Fig. 9b), and MPC structure in matrix-facing state (Nb2-bound) is highly similar to a SemiSWEET structure in outward-open conformation (Extended Data Fig. 9c). These comparisons suggest that transporters composed of a similar 1-3-2 triple helix bundle may share a similar alternating access mechanism for substrate transport. However, unlike SemiSWEET, which possesses a spacious putative sugar binding pocket in the occluded state (Extended Data Fig. 9d), the putative pyruvate binding pocket in MPC is notably small (Fig. 2c). By comparing the pocket-forming residues between the two occluded structures, we found that in MPC, several residues with large side chains orient towards the transport path, thus creating a much smaller pocket compared to that in SemiSWEET (Extended Data Fig. 9e). These analyses highlight the structural adaptations for different substrates among transporters with the same protein fold.

Taken together, our study provides a comprehensive and mechanistic understanding for mitochondrial pyruvate carrier and offers valuable insights into the substrate transport mechanisms of other homologous transporters. Furthermore, our research will also greatly promote the development of drugs targeting MPC for the treatment of related human diseases.

References

1 Bricker, D. K. *et al.* A mitochondrial pyruvate carrier required for pyruvate uptake in yeast, Drosophila, and humans. *Science* **337**, 96-100, doi:10.1126/science.1218099 (2012).

2 Herzig, S. *et al.* Identification and functional expression of the mitochondrial pyruvate carrier. *Science* **337**, 93-96, doi:10.1126/science.1218530 (2012).

3 Gray, L. R., Tompkins, S. C. & Taylor, E. B. Regulation of pyruvate metabolism and human disease. *Cell Mol Life Sci* **71**, 2577-2604, doi:10.1007/s00018-013-1539-2 (2014).

4 Vanderperre, B., Bender, T., Kunji, E. R. & Martinou, J. C. Mitochondrial pyruvate import and its effects on homeostasis. *Curr Opin Cell Biol* **33**, 35-41, doi:10.1016/j.ceb.2014.10.008 (2015).

5 Vanderperre, B. *et al.* MPC1-like Is a Placental Mammal-specific Mitochondrial Pyruvate Carrier Subunit Expressed in Postmeiotic Male Germ Cells. *J Biol Chem* **291**, 16448-16461, doi:10.1074/jbc.M116.733840 (2016).

6 Bender, T. & Martinou, J. C. The mitochondrial pyruvate carrier in health and disease: To carry or not to carry? *Biochim Biophys Acta* **1863**, 2436-2442, doi:10.1016/j.bbamcr.2016.01.017 (2016).

7 Halestrap, A. P. Pyruvate and ketone-body transport across the mitochondrial membrane. Exchange properties, pH-dependence and mechanism of the carrier. *Biochem J* **172**, 377-387, doi:10.1042/bj1720377 (1978).
8 Tavoulari, S. *et al.* The yeast mitochondrial pyruvate carrier is a hetero-dimer in its functional state. *Embo j* **38**, doi:10.15252/embj.2018100785 (2019).
9 Schell, J. C. *et al.* A role for the mitochondrial pyruvate carrier as a repressor of the Warburg effect and colon cancer cell growth. *Mol Cell* **56**, 400-413, doi:10.1016/j.molcel.2014.09.026 (2014).
10 Compan, V. *et al.* Monitoring Mitochondrial Pyruvate Carrier Activity in Real Time Using a BRET-Based Biosensor: Investigation of the Warburg Effect. *Mol Cell* **59**, 491-501, doi:10.1016/j.molcel.2015.06.035 (2015).
11 Porcelli, A. M. *et al.* pH difference across the outer mitochondrial membrane measured with a green fluorescent protein mutant. *Biochem Biophys Res Commun* **326**, 799-804, doi:10.1016/j.bbrc.2004.11.105 (2005).
12 Vander Heiden, M. G., Cantley, L. C. & Thompson, C. B. Understanding the Warburg effect: the metabolic requirements of cell proliferation. *Science* **324**, 1029-1033, doi:10.1126/science.1160809 (2009).
13 Liberti, M. V. & Locasale, J. W. The Warburg Effect: How Does it Benefit Cancer Cells? *Trends Biochem Sci* **41**, 211-218, doi:10.1016/j.tibs.2015.12.001 (2016).
14 Bader, D. A. *et al.* Mitochondrial pyruvate import is a metabolic vulnerability in androgen receptor-driven prostate cancer. *Nat Metab* **1**, 70-85, doi:10.1038/s42255-018-0002-y (2019).
15 Elia, I. *et al.* Breast cancer cells rely on environmental pyruvate to shape the metastatic niche. *Nature* **568**, 117-121, doi:10.1038/s41586-019-0977-x (2019).
16 Ruiz-Iglesias, A. & Mañes, S. The Importance of Mitochondrial Pyruvate Carrier in Cancer Cell Metabolism and Tumorigenesis. *Cancers (Basel)* **13**, doi:10.3390/cancers13071488 (2021).
17 McCommis, K. S. *et al.* Nutritional modulation of heart failure in mitochondrial pyruvate carrier-deficient mice. *Nat Metab* **2**, 1232-1247, doi:10.1038/s42255-020-00296-1 (2020).
18 Fernandez-Caggiano, M. & Eaton, P. Heart failure-emerging roles for the mitochondrial pyruvate carrier. *Cell Death Differ* **28**, 1149-1158, doi:10.1038/s41418-020-00729-0 (2021).
19 Ghosh, A. *et al.* Mitochondrial pyruvate carrier regulates autophagy, inflammation, and neurodegeneration in experimental models of Parkinson's disease. *Sci Transl Med* **8**, 368ra174, doi:10.1126/scitranslmed.aag2210 (2016).
20 Quansah, E. *et al.* Targeting energy metabolism via the mitochondrial pyruvate carrier as a novel approach to attenuate neurodegeneration. *Mol Neurodegener* **13**, 28, doi:10.1186/s13024-018-0260-x (2018).
21 Divakaruni, A. S. *et al.* Inhibition of the mitochondrial pyruvate carrier protects from excitotoxic neuronal death. *J Cell Biol* **216**, 1091-1105, doi:10.1083/jcb.201612067 (2017).

22 McCommis, K. S. *et al.* Targeting the mitochondrial pyruvate carrier attenuates fibrosis in a mouse model of nonalcoholic steatohepatitis. *Hepatology* **65**, 1543-1556, doi:10.1002/hep.29025 (2017).
23 Gray, L. R. *et al.* Hepatic Mitochondrial Pyruvate Carrier 1 Is Required for Efficient Regulation of Gluconeogenesis and Whole-Body Glucose Homeostasis. *Cell Metab* **22**, 669-681, doi:10.1016/j.cmet.2015.07.027 (2015).
24 Zhu, B. *et al.* Inhibition of the mitochondrial pyruvate carrier simultaneously mitigates hyperinflammation and hyperglycemia in COVID-19. *Sci Immunol* **8**, eadf0348, doi:10.1126/sciimmunol.adf0348 (2023).
25 Corbet, C. *et al.* Interruption of lactate uptake by inhibiting mitochondrial pyruvate transport unravels direct antitumor and radiosensitizing effects. *Nat Commun* **9**, 1208, doi:10.1038/s41467-018-03525-0 (2018).
26 Halestrap, A. P. The mitochondrial pyruvate carrier. Kinetics and specificity for substrates and inhibitors. *Biochem J* **148**, 85-96, doi:10.1042/bj1480085 (1975).
27 Bender, T., Pena, G. & Martinou, J. C. Regulation of mitochondrial pyruvate uptake by alternative pyruvate carrier complexes. *Embo j* **34**, 911-924, doi:10.15252/embj.201490197 (2015).
28 Xu, Y. *et al.* Structures of bacterial homologues of SWEET transporters in two distinct conformations. *Nature* **515**, 448-452, doi:10.1038/nature13670 (2014).
29 Wang, J. *et al.* Crystal structure of a bacterial homologue of SWEET transporters. *Cell Res* **24**, 1486-1489, doi:10.1038/cr.2014.144 (2014).
30 Lee, Y., Nishizawa, T., Yamashita, K., Ishitani, R. & Nureki, O. Structural basis for the facilitative diffusion mechanism by SemiSWEET transporter. *Nat Commun* **6**, 6112, doi:10.1038/ncomms7112 (2015).
31 Paradies, G. & Ruggiero, F. M. Age-related changes in the activity of the pyruvate carrier and in the lipid composition in rat-heart mitochondria. *Biochim Biophys Acta* **1016**, 207-212, doi:10.1016/0005-2728(90)90060-h (1990).
32 Halestrap, A. P. The mechanism of the inhibition of the mitochondrial pyruvate transportater by alpha-cyanocinnamate derivatives. *Biochem J* **156**, 181-183, doi:10.1042/bj1560181 (1976).
33 Halestrap, A. P. Stimulation of pyruvate transport in metabolizing mitochondria through changes in the transmembrane pH gradient induced by glucagon treatment of rats. *Biochem J* **172**, 389-398, doi:10.1042/bj1720389 (1978).
34 Yang, C. *et al.* Glutamine oxidation maintains the TCA cycle and cell survival during impaired mitochondrial pyruvate transport. *Mol Cell* **56**, 414-424, doi:10.1016/j.molcel.2014.09.025 (2014).
35 Vacanti, N. M. *et al.* Regulation of substrate utilization by the mitochondrial pyruvate carrier. *Mol Cell* **56**, 425-435, doi:10.1016/j.molcel.2014.09.024 (2014).
36 Tavoulari, S. *et al.* Key features of inhibitor binding to the human mitochondrial pyruvate carrier hetero-dimer. *Mol Metab* **60**, 101469, doi:10.1016/j.molmet.2022.101469 (2022).

37 Hildyard, J. C., Ammälä, C., Dukes, I. D., Thomson, S. A. & Halestrap, A. P. Identification and characterisation of a new class of highly specific and potent inhibitors of the mitochondrial pyruvate carrier. *Biochim Biophys Acta* **1707**, 221-230, doi:10.1016/j.bbabio.2004.12.005 (2005).

38 Halestrap, A. P. & Denton, R. M. The specificity and metabolic implications of the inhibition of pyruvate transport in isolated mitochondria and intact tissue preparations by alpha-Cyano-4-hydroxycinnamate and related compounds. *Biochem J* **148**, 97-106, doi:10.1042/bj1480097 (1975).

Methods

Constructs design and expression of MPC

The cDNAs of human MPC1 and MPC2 were separately cloned into pCAG vectors with a C-terminal HA-tag for MPC1 and a C-terminal 3xFLAG-tag for MPC2. During co-expression, plasmids containing cDNAs of MPC1 and MPC2 were co-transfected into Expi293F cells (Thermo Fisher Scientific). After transfection, cells were cultured in Multitron shaker at 37 °C, 125 rpm, 8% CO_2, and 80% humidity for 60 hrs.

Mitochondria isolation and MPC purification

The transfected cells for recombinant overexpression of MPC complex were harvested and resuspended in Buffer A (83 mM sucrose, 20 mM HEPES pH 7.4). Resuspended cells were frozen by liquid nitrogen and thawed by water bath at room temperature followed by gentle sonication for cell lysis. A two-fold dilution of cell lysate was achieved by adding equal volume of Buffer B (250 mM sucrose, 20 mM HEPES pH 7.4). After centrifugation at 700 g for 8 mins, cell debris and nuclei were pelleted. The supernatant was then subjected to centrifugation at 12,000 g for 1 hr.

The obtained crude mitochondria pellet was resuspended in solubilization buffer (150 mM NaCl, 20 mM HEPES pH 7,4, 10% glycerol) supplemented with protease inhibitors cocktail. Membrane proteins were extracted from above crude mitochondria suspension by adding detergents at final concentration of 1% (w/v) lauryl maltose neopentyl glycol (LMNG) and 0.1% (w/v) cholesteryl hemisuccinate (CHS). After gentle stirring at 4 °C for 2 hrs, the lysate was cleared by centrifugation at 30,000 g for 1 hr before removal of the insoluble fraction.

Supernatant was collected and loaded onto anti-FLAG agarose resin (GenScript) in gravity column (Bio-Rad). The resin was washed by 50 column volumes with wash buffer (150 mM NaCl, 20 mM HEPES pH 7.4, 0.01% LMNG and 0.001% CHS). Proteins were then eluted by wash buffer supplemented with 0.5 mg/mL 3xFLAF peptide. Each protein solution was concentrated and subjected to further purification by size-exclusion chromatography (SEC) on a Superdex 200 Increase 10/300 GL column (Cytiva) with buffer containing 150 mM NaCl, 0.01% LMNG, 0.001% CHS and 20 mM of a desired pH buffer according to different purposes.

In vitro selection of MPC-specific nanobodies

The procedure of obtaining MPC-specific nanobodies was similar as previously described[39]. One round of ribosome display and three rounds of phage display were performed before single clone selection via ELISA.

For ribosome display, *in vitro* translation of five home-made synthetic nanobody mRNA libraries were performed using PURExpress2.1 kit (GeneFrontier). 80 nM of biotinylated MPC was added to the diluted reaction to start solution panning. Bound nanobodies with their corresponding mRNAs were captured by pulling down biotinylated MPC with pre-blocked Dynabeads MyOne Streptavidin T1 (Invitrogen). After elution, mRNAs were purified, reverse transcribed and then amplified by PCR using customized primers. The PCR products were cloned into a phage display vector modified based on pDX_init[39] and transformed into SS320 cells via electroporation. Phage library was produced by bacteria culture containing the nanobody library with the help of M13KO7 helper phage (NEB).

The first round of phage display was performed in 96-well plates. 50 nM of biotinylated MPC was incubated with purified phages (10^{12} phages/mL in 5 ml) on ice for 20 mins. Then the panning solution was added into pre-blocked NeutrAvidin-coated 96-well plates (Nunc Maxisorp, Merck) and incubated for 15 mins. The wells were washed before phages elution using mild trypsin digestion. SS320 cells were infected by eluted phages to amplify phages for a second round of display, during which, 80 nM of biotinylated MPC were incubated with purified phages in panning solution on ice for 20 mins. Bound phages were then captured by

pre-blocked Dynabeads MyOne Streptavidin C1 (Invitrogen). After washing, weakly associated phages were removed by adding 2 μM of non-biotinylated MPC for incubation on ice for 6 mins. Phages were eluted and used as seeds for the third round of display, which was similar to the second round except that: phages were pre-incubated with empty pre-blocked beads to remove streptavidin binders; the concentration of biotinylated MPC was reduced to 50 nM; and no off-rate step was performed. The final phagemid was extracted (QIAprep Spin Miniprep Kit, Qiagen). DNA fragments encoding enriched nanobodies were cloned into the expression vector pET26b with an N-terminal pelB signal sequence and a C-terminal His-tag. ELISA was used to identify positive clones for sequencing.

Expression and purification of nanobodies

Positive clones were transformed into *E.coli* BL21 competent cells and nanobody overexpression was induced by 1 mM isopropyl-β-d-thiogalactoside (IPTG) for 16 hrs at 22 °C in TB medium. Nanobodies were extracted by osmotic shock from the periplasmic space. Specifically, each cell pellet from 50 mL culture was resuspended with 5 mL of periplasmic extraction buffer containing 0.5 M sucrose, 0.2 M Tris-HCl pH 8.0, 0.5 mM EDTA before 10 ml of water was added to start extraction at 4°C for 1 hr. After incubation, 2 mM $MgCl_2$, 20 mM imidazole, and 300 mM NaCl were supplemented into the suspension. The extract was cleared by centrifugation at 8,000 g for 20 mins. The supernatant was incubated with 200 ul of Ni-NTA Superflow (Smart-Lifesciences) for 1 hr at 4°C before transferred to an empty gravity column and washed with Washing Buffer (25 mM HEPES pH 7.4, 300 mM NaCl, 25 mM imidazole). Nanobodies were eluted with Washing Buffer supplemented with 400 mM imidazole. Eluted proteins were further purified on Superdex 75 10/300 (Cytiva) in buffer containing 25 mM HEPES pH7.4, 150 mM NaCl and 5% glycerol.

Nanobody Characterization

The binding properties of the nanobodies were characterized using both Biolayer Interferometry (BLI, ForteBio Octet Red96e) and pull-down assays. In BLI analysis, we evaluated the affinities of the nanobodies for MPC in two states, substrate-bound and inhibitor-

519 bound. MPC was pre-incubated with sodium pyruvate or UK5099 for 30 mins on ice. The NTA
520 biosensor (Sartorius) was used to immobilize His-tagged nanobodies, and MPC at a
521 concentration of 500nM was allowed to bind and dissociate from the biosensor. The assay
522 buffer contained 20 mM HEPES pH 7.4, 150 mM NaCl, 0.01% LMNG, 0.001% CHS, 10 mM
523 imidazole, with either 500 μM UK5099 or 2 mM sodium pyruvate supplemented.

524 During pull-down assay, we examined MPC in both pyruvate-bound and inhibitor-bound
525 states using His-tagged nanobody as bait. MPC was diluted to 1.8 μM in 50 ul of assay buffer
526 (same as above but without imidazole) for incubation on ice for 30 mins. Then, an equal molar
527 of nanobodies was added to incubate for another 30 mins. The pull-down procedure was
528 performed using 10 μl of pre-washed Anti-DYKDDDDK G1 Affinity resin (GenScript), followed
529 by washing and elution steps. The eluted proteins were analyzed by SDS-PAGE.

530 **Cryo-EM sample preparation and data acquisition**

531 Apo, pyruvate-bound and UK5099-bound MPC complexes were purified with SEC buffers
532 containing 20 mM Tris-HCl pH8.0, HEPES pH 6.8 and HEPES pH 7.4, respectively. During
533 purification of pyruvate-treated MPC, 2 mM pyruvate was supplemented since the extraction
534 step. For UK5099-bound MPC purification, SEC buffer was supplemented with 100 μM
535 UK5099. To obtain MPC-Nb1 and Nb1-MPC-Nb2 complexes, each nanobody was added to
536 purified MPC at 1.5: 1 molar ratio and incubated overnight at 4 °C. The resulting samples were
537 further purified by SEC. Peak fractions were collected and concentrated to ~ 4-5 mg/ mL for
538 cryo-EM grids preparation.

539 Protein samples as mentioned above were applied to glow-discharged holey carbon-
540 coated grids (Quantifoil 300 mesh, Au R1.2/1.3) for 30 s. The grids were blotted for 4.5 s at
541 100% relative humidity at a chamber temperature of 4 °C then plunge-frozen in liquid ethane
542 for flash freezing using Vitrobot Mark IV (Thermo Fisher Scientific). Image acquisitions were
543 performed on Titan Krios G4 (FEI) operating at 300 kV with a Selectris X imaging filter (Thermo
544 Fisher Scientific) and Falcon 4i direct electron detector (Thermo Fisher Scientific). Data were
545 collected in counted super-resolution mode at magnification of 215,000 x, physical pixel size

of 0.57 Å. Movie stacks were automatically acquired using Thermo Scientific EPU (Thermo Fisher Scientific) with a 20 eV slit width and a defocus range from −0.8 to − 1.2 μm. The movies were stored as EER format which were exposed for 2.45 s with total dose of ~50 e^{-}/Å^2.

Cryo-EM data processing

The image processing workflows are illustrated in Extended Data Figs. 2，3c. Motion-correction and dose weighting were performed using Patch Motion Correction in cryoSPARC[40]. Contrast transfer function (CTF) parameters were estimated with Patch-CTF in cryoSPAR[40]. Micrographs with CTF fitting resolution worse than 6 Å were excluded during manual curation. Initial particles were picked from few partial micrographs using blob picker in cryoSPARC[40] and 2D averages were generated. Final particle picking was done by template picker using templates from those 2D results. Particles were extracted using a box size of 320 pixels and cropped into 20 pixels, 40 pixels, 80 pixels, 160 pixels respectively to speed up early calculation steps.

For dataset of the apo MPC in complex with Nb1 in IMS-open state (pH 8.0), 1997 k particles were extracted from 6948 micrographs with pixel size of 9.12 Å (box size 20 pixels), After one round of 2D classification, the good particles were re-extracted and re-centered with pixel size of 4.56 Å (box size 40 pixels) for the next round of 2D classification. Above process was continued until the particles were re-extracted with pixel size of 1.14 Å (box size 160 pixels). After 4 rounds of 2D classification to remove obvious junk, a total of 479 k particles were retained. This data set was then used for ab-initio reconstruction, with carefully tuning parameters including the number of classes, initial resolution, initial and final minibatch sizes using cryoSPARC[40]. A resulting map with clear transmembrane helices was generated from a 4 classes ab-initio reconstruction. After non-uniform (NU) refinement[41], a good reference at 3.7 Å resolution was generated for the next 3D classification. Another 4201 k particles were extracted from 14604 new micrographs and were combined with above 1997 k particles. After 4 rounds of 2D classification, 886k particles (1.14 Å pixel size) were used for hetero refinement, and the map with a resolution of 3.7 Å was imported as a good reference. A map with a resolution of 3.3 Å was reconstructed using 223 k particles, after 3 rounds of hetero refinement

and NU-refinement. To further improve the resolution, seed-facilitated 3D classification[42] was performed. A dataset containing 3487k particles was re-extracted with pixel size of 0.57 Å (box size 320 pixels), which was used as the seed pool. The above 223k particles were also re-extracted with pixel size of 0.57 Å (box size 320 pixels), and were used as seeds for seed-facilitated 3D classification. After seed-facilitated 3D classification, hetero refinement and NU-refinement, a final map at an average resolution of 3.2 Å was reconstructed by 474 k particles.

For dataset of the apo MPC in complex with Nb1 in IMS-open state (pH 6.8), 2, 411 k particles were extracted from 7, 340 micrographs with pixel size of 9.12 Å (box size 20 pixels). The same 2D classification strategy as the apo MPC-Nb1 complex in IMS-open state (pH 8.0) dataset was performed. After that, 404 k particles with pixel size of 1.14 Å were used for ab-initio reconstruction, and a good class containing 128 k particles was selected. After NU-refinement，a map at 3.9 Å resolution was generated. Another 3, 201 k particles were extracted from 8, 809 micrographs and were combined with above 2, 411 k particles. After 1 round of 2D classification, the resulting 2, 344 k particles were re-extracted with pixel size of 0.57 Å (box size 320 pixels). The above 128 k particles were imported as seeds into the dataset of the 2, 344 k particles. After seed-facilitated 3D classification, multiple hetero refinement and NU-refinement, a map with a resolution of 3.7 Å was reconstructed using 445 k particles. These particles were subjected to 2 rounds of hetero refinement, ab-initio reconstruction and NU-refinement, which resulted in a final map at 3.4 Å resolution.

For the dataset of pyruvate-treated MPC in complex with Nb1 in IMS-open state (pH 8.0), 8, 183 k particles were extracted from 27, 987 micrographs with pixel size of 9.12 Å (box size 20 pixels). The same 2D classification strategy as the apo MPC-Nb1 complex in IMS-open state (pH 8.0) dataset was performed. The remaining 947 k particles with pixel size of 1.14 Å were used for ab-initio reconstruction. A resulting map with clear transmembrane helices was generated from a 5 classes ab-initio reconstruction. After NU-refinement, a good reference at 3.8 Å resolution was generated by 284 k particles. These particles were re-extracted with pixel size of 0.57 Å (box size 320 pixels). A dataset containing 5, 476 k particles were also re-extracted with pixel size of 0.57 Å (box size 320 pixels). The 284 k particles were imported as

seeds into the dataset of the 5, 476 k particles. After seed-facilitated 3D classification, 1, 026 k particles were subjected to NU-refinement, which resulted in a map at 3.5 Å resolution. After 2 rounds of hetero refinement, ab-initio reconstruction and NU-refinement, the MPC-Nb1 complex in intermediate state (pyruvate-treated, pH 8.0) dataset gave rise to a reconstruction at an average resolution of 3.4 Å.

For the dataset of pyruvate-treated MPC in complex with Nb1 in occluded state (pH 6.8), 12, 865 k particles were extracted from 40, 380 micrographs with pixel size of 9.12 Å (box size 20 pixels). The same 2D classification strategy as the apo MPC-Nb1 complex in IMS-open state (pH 8.0) dataset was performed. After that, 1, 347 k particles with pixel size of 1.14 Å were used for 2 rounds of ab-initio reconstruction & hetero refinement respectively, and a good class containing 405 k particles was selected for the further ab-initio reconstruction. Through 3D classification, intermediate state maps were reconstructed using 69 % of the 405 k particles, and a ‘ apo ’ like state was reconstructed using remaining ~30 % of the particles. The particles belong to the intermediate state were re-extracted with pixel size of 0.57 Å (box size 320 pixels). Another 4, 472 k particles were extracted from 12, 783 new micrographs and were combined with above 12, 865 k particles. After 1 round of 2D classification, the resulting 7, 289 k particles were re-extracted with pixel size of 0.57 Å (box size 320 pixels). The above particles belong to the intermediate state were imported as seeds into the dataset of the 7, 289 k particles. After seed-facilitated 3D classification, multiple hetero refinement, and NU-refinement, a map with a resolution of 3.9 Å was reconstructed using 472 k particles. To further improve the resolution, ab-initio reconstruction and hetero refinement were performed. The resulting 312 k particles were subjected to NU-refinement, yielding a final map with the resolution of 3.7 Å.

For the dataset of MPC-Nb1 complex in UK5099-bound state, 1665 k particles were extracted from 6614 micrographs with pixel size of 9.12 Å (box size 20 pixels). The same 2D classification strategy as apo MPC-Nb1 complex in IMS-open state (pH 8.0) dataset was performed. After that, 222 k particles with pixel size of 1.14 Å were used for ab-initio reconstruction, and a good class containing 69 k particles was selected for the next 3D

classification. Another 29743 micrographs were combined with above 6614 micrographs, from which a total of 9473 k particles were extracted with pixel size of 9.12 Å (box size 20 pixels). These particles were subjected to 5 rounds of 2D classification and 932 k particles with pixel size of 1.14 Å were remained. The map generated by above 69 k particles was used as a good reference for the hetero refinement of the 932 k particles. After 3 rounds of hetero refinement, ab-initio reconstruction and NU-refinement, a map with a resolution of 3.6 Å was reconstructed using 184 k particles. These particles were imported as seeds into the dataset of 9473 k particles, all particles for seeding were re-extracted with pixel size of 0.57 Å (box size 320 pixels). After 2 rounds of seed-facilitated 3D classification, 1639 k particles were subjected to NU-refinement, which resulted in a map at 3.3 Å resolution. After 2 rounds of hetero refinement, ab-initio reconstruction and NU-refinement, the MPC-Nb1 complex in the UK5099-bound state dataset gave rise to a reconstruction at an average resolution of 3.2 Å.

For the dataset of pyruvate-treated MPC in complex with Nb1 and Nb2 in matrix-facing state (pH 6.8), 10, 642 k particles were extracted from 31195 micrographs with pixel size of 9.12 Å (box size 20 pixels). The same 2D classification strategy as the apo MPC-Nb1 complex in IMS-open state (pH 8.0) dataset was performed. The remaining 1197 k particles with pixel size of 1.14 Å were used for ab-initio reconstruction. A class that showed obvious secondary structure features were selected and subjected to additional 2 rounds of hetero refinement and NU-refinement, which resulted in a map with a resolution of 3.2 Å containing 300 k particles. These particles were re-extracted with pixel size of 0.57 Å (box size 320 pixels). Another 10, 882 k particles were extracted from 30067 new micrographs and were combined with above 10, 642 k particles. After 1 round of 2D classification, the resulting 14,254 k particles were re-extracted with pixel size of 0.57 Å (box size 320 pixels). The above 300 k particles were imported as seeds into the dataset of the 14,254 k particles. After seed-facilitated 3D classification, and NU-refinement, a map with a resolution of 3.2 Å was reconstructed using 2296 k particles. To further improve the resolution, 2 rounds of 3D classification using good and biased references or references with resolution gradients were

performed. The resulting 1023 k particles were subjected to NU-refinement, yielding a final map with the resolution of 3.0 Å.

Model building and refinement.

The initial structure models for MPC and nanobodies were generated by AlphaFold2[43]. The structure was docked into the density map and manually adjusted and re-built by COOT[44]. Model refinement was performed using phenix.real_space_refine in PHENIX[45]. For cross-validations, the model vs. map Fourier Shell Correlation (FSC) curves were generated in the Comprehensive Validation module in PHENIX. The structures of all states were validated through examination of the Molprobity scores[46], and statistics of the Ramachandran plots. Local resolutions were estimated using cyroSPARC[40] local resolution estimation. Structure Figures were produced using PyMOL (http://www.pymol.org), UCSF Chimera[47] and ChimeraX[48].

Proteoliposomes reconstitution

The MPC complexes were reconstituted into liposomes as previously established with modifications[8]. Briefly, egg L-a-phosphatidylcholine (Sigma) and tetraoleoyl cardiolipin (Sigma) were dissolved into methanol at a 20:1 (w/w) ratio. Solvent was removed through drying by nitrogen gas. Above dissolving and drying procedure was performed twice. The prepared lipids were resuspended by buffer containing 20 mM Tris-HCl pH 8.0 and 100 mM NaCl to a final concentration of 15 mg/mL. Lipids were further solubilized with 1.2% (v/v) pentaethylene glycol monododecyl ether (Sigma), and purified protein was added at a lipid-to-protein ratio of 60:1 (w/w) following by incubation for 2 hrs at 4 °C. Pentaethylene glycol monododecyl ether and detergents from protein samples were removed by Bio-Beads SM-2 (Bio-Rad) during the proteoliposomes formation. Samples were then extruded through 0.4 μm filter (Cytiva) by extruder (Avanti). Proteoliposomes were harvested by centrifugation at 120,000 g for 1 hr. The pelleted proteoliposomes were resuspended in buffer containing 20 mM Tris-HCl pH 8.0 and 100mM NaCl at a final protein concentration of 0. 5 mg/mL.

[^{14}C]-Pyruvate transport assay

The pyruvate transport activity was measured by [^{14}C]-Pyruvate uptake assays described previously with modifications[2,8]. To initiate transport, the proteoliposomes were diluted 100 folds in external buffer containing 50 μM [^{14}C]-pyruvate (Revvity, Product Number: NEC256, specific activity: 10.7 mCi/mmol) at room temperature. The external buffers of different pH containing 50 μM [^{14}C]-pyruvate were chosen accordingly (20 mM MES pH 6.4, 100 mM NaCl or 20 mM Tris-HCl pH 8.0, 100 mM NaCl). After transport for 30 s, reactions were immediately terminated by addition of UK5099 at final concentration of 1 mM. Samples were then rapidly filtrated through cellulose nitrate 0.22-μm filters (Millipore) followed by triple washes with 0.8 ml of ice-cold internal buffer (20 mM Tris-HCl pH 8.0, 100 mM NaCl). Each filter was placed into 24-well plate (Perkin Elmer) and overnight dissolved in 800 μl of Ultima Gold scintillation liquid (Perkin Elmer). Scintillation counting was performed using MicroBeta2® Microplate Counter (Perkin Elmer). Empty liposomes without MPC were used as control. Standard calibration curve was made with CPM values read from [^{14}C]-pyruvate of 4.5 pmol, 45 pmol, 450 pmol and 4.5 nmol in 800 μL Ultima Gold scintillation liquid (Perkin Elmer). For the time course measurement of pyruvate transport activity by WT (MPC1/2) in proteoliposome and empty liposomes measured by [^{14}C]-pyruvate uptake assay. Imported pyruvate was quantified by scintillation counting at uptake duration of 0s, 10s, 20s, 30s, 60s, 120s and 180s. To determine the K_m value, reactions were initiated by adding a series of [^{14}C]-Pyruvate concentration (25 μM, 50 μM, 100 μM, 200 μM, 400 μM and 600 μM). K_m value was calculated by fitting to the Michaelis–Menten equation in GraphPad Prism 10. For dose-dependent inhibition assay, proteoliposomes were pre-incubated with UK5099 at different concentrations (0.001nM, 10 nM, 50 nM, 100 nM, 500 nM, 1 μM, 5 μM, 10 μM, 50 μM and 100 μM) for 1 min at room temperature before the reaction initiated by addition of 50 μM [^{14}C]-pyruvate. The IC_{50} values were determined using nonlinear regression fittings using GraphPad Prism 10.

Microscale thermophoresis (MST) binding assay

The binding affinity of MPC variants towards UK5099 was measured using the Monolith NT.115 from NanoTemper Technologies. The purified C-terminal 8 ×His-tagged MPC1/MPC2 was diluted with buffer containing 20 mM HEPES 7.4, 150 mM NaCl, and 0.01% LMNG+ 0.001%

CHS (w/v). MPC proteins were fluorescently labelled with RED-tris-NTA 2nd generation dye (NanoTemper technologies) according to the manufacturer's protocol and about 50 nM of labelled protein was used for each assay. UK5099 with serial dilutions up to 2 μM or 300 μM were mixed with indicated protein. After incubating at room temperature for 30 minutes, the samples were loaded into NanoTemper glass capillaries. Measurements were performed using 40% LED excitation and medium MST power settings. The MST data was further analyzed by Monolith NT.115.

Computational inhibitor docking

All protein residues in the cryo-EM structure of MPC in complex with UK5099 were extracted as the receptor model, to which hydrogens were added with PyMol. The model was then prepared for docking using ADFR suite v1.0[49]. Briefly, the model was converted to PDBQT file by prepare_receptor; grid maps were generated using AutoGrid v4.2.7[50], and a large grid box centered at the hydroxyl oxygen of Tyr62 with grid dimensions of 160 Å x 80 Å x 80 Å and 0.375 Å spacing was specified to cover the entire protein. The last sidechain dihedrals of the pocket-surrounding residues (chain A: Asn33, Tyr62, Phe66, Phe69, Leu80; chain B: Trp82, Leu96, Asn100) were set as flexible. The SDF files of all the ligands were obtained from PubChem[51]. The protonation states of the ligands were corrected using OpenBabel v3.1.0[52] with pH 7.4, and Meeko v0.5.1[53] was used to prepare the ligands for docking. Docking was performed using AutoDock-Vina v1.2.5[54,55] with default parameters, except that exhaustiveness were set to 128 and the maximum number of generated binding modes were set to 100.

Data availability

Atomic coordinates and corresponding EM maps of the structures of apo MPC in complex with Nb1 at pH 8.0 (PDB ID: 8YW6 and EMDB ID: EMD-39624) and pH 6.8 (PDB ID: 9KNW and EMDB ID: EMD-62464) in IMS-open state, structure of pyruvate-treated MPC in complex with Nb1 at pH 8.0 in IMS-open state (PDB ID: 9KNY and EMDB ID: EMD-62466), structure of pyruvate-treated MPC in complex with Nb1 at pH 6.8 in occluded state (PDB ID: 9KNX and

EMDB ID: EMD-62465), structure of pyruvate-treated MPC in complex with Nb1 and Nb2 at pH 6.8 in matrix-facing/inhibitory state (PDB ID : 8YW9 and EMDB ID : EMD-39626), and UK5099-bound structure (PDB ID : 8YW8 and EMDB ID : EMD-39625) have been deposited in the Protein Data Bank (http://www.rcsb.org) and the Electron Microscopy Data Bank (https://www.ebi.ac.uk/pdbe/emdb/), respectively. The SemiSWEET structures used for structural comparisons with MPC in Extended Data Fig. 9 are accessible in the Protein Data Bank with PDB codes of 4X5M, 4RNG, 4QNC and 4QND.

methods references

39 Zimmermann, I. *et al.* Generation of synthetic nanobodies against delicate proteins. *Nat Protoc* **15**, 1707-1741, doi:10.1038/s41596-020-0304-x (2020).

40 Punjani, A., Rubinstein, J. L., Fleet, D. J. & Brubaker, M. A. cryoSPARC: algorithms for rapid unsupervised cryo-EM structure determination. *Nat Methods* **14**, 290-296, doi:10.1038/nmeth.4169 (2017).

41 Punjani, A., Zhang, H. & Fleet, D. J. Non-uniform refinement: adaptive regularization improves single-particle cryo-EM reconstruction. *Nat Methods* **17**, 1214-1221, doi:10.1038/s41592-020-00990-8 (2020).

42 Wang, N. *et al.* Structural basis of human monocarboxylate transporter 1 inhibition by anti-cancer drug candidates. *Cell* **184**, 370-383 e313, doi:10.1016/j.cell.2020.11.043 (2021).

43 Jumper, J. *et al.* Highly accurate protein structure prediction with AlphaFold. *Nature* **596**, 583-589, doi:10.1038/s41586-021-03819-2 (2021).

44 Emsley, P. & Cowtan, K. Coot: model-building tools for molecular graphics. *Acta Crystallogr D Biol Crystallogr* **60**, 2126-2132, doi:10.1107/s0907444904019158 (2004).

45 Afonine, P. V. *et al.* Real-space refinement in PHENIX for cryo-EM and crystallography. *Acta Crystallogr D Struct Biol* **74**, 531-544, doi:10.1107/S2059798318006551 (2018).

46 Davis, I. W. *et al.* MolProbity: all-atom contacts and structure validation for proteins and nucleic acids. *Nucleic Acids Res* **35**, W375-383, doi:10.1093/nar/gkm216 (2007).

47 Pettersen, E. F. *et al.* UCSF Chimera--a visualization system for exploratory research and analysis. *J Comput Chem* **25**, 1605-1612, doi:10.1002/jcc.20084 (2004).

48 Pettersen, E. F. *et al.* UCSF ChimeraX: Structure visualization for researchers, educators, and developers. *Protein Sci* **30**, 70-82, doi:10.1002/pro.3943 (2021).

49 Ravindranath, P. A., Forli, S., Goodsell, D. S., Olson, A. J. & Sanner, M. F. AutoDockFR: Advances in Protein-Ligand Docking with Explicitly Specified Binding Site Flexibility. *PLoS Comput Biol* **11**, e1004586, doi:10.1371/journal.pcbi.1004586 (2015).

50 Zhang, Y., Forli, S., Omelchenko, A. & Sanner, M. F. AutoGridFR: Improvements on AutoDock Affinity Maps and Associated Software Tools. *Journal of computational chemistry* **40**, 2882-2886, doi:10.1002/jcc.26054 (2019).

51 Kim, S. *et al.* PubChem 2023 update. *Nucleic Acids Research* **51**, D1373-D1380, doi:10.1093/nar/gkac956 %J Nucleic Acids Research (2022).

52 O'Boyle, N. M. *et al.* Open Babel: An open chemical toolbox. *Journal of Cheminformatics* **3**, 33, doi:10.1186/1758-2946-3-33 (2011).

53 Meeko: Preparation of small molecules for AutoDock (Forli Lab, 2022); https://pypi.org/project/meeko/.

54 Eberhardt, J., Santos-Martins, D., Tillack, A. F. & Forli, S. AutoDock Vina 1.2.0: New Docking Methods, Expanded Force Field, and Python Bindings. *J Chem Inf Model* **61**, 3891-3898, doi:10.1021/acs.jcim.1c00203 (2021).

55 Trott, O. & Olson, A. J. AutoDock Vina: improving the speed and accuracy of docking with a new scoring function, efficient optimization, and multithreading. *Journal of computational chemistry* **31**, 455-461, doi:10.1002/jcc.21334 (2010).

Acknowledgements

We would like to thank the following facilities at Westlake University: Cryo-EM Facility for providing cryo-EM support, High-Performance Computing Center for computational resources and related assistance, and the radioisotope laboratory for providing related facilities and assistance. We thank Dr. Qi Hu for discussion about the project and revision on manuscript draft. This work was supported by Ministry of Science and Technology of China, National Key R&D Program (Project No. 2022YFA1303700). This work was also supported by Key R&D Program of Zhejiang（2024SSYS0029）and Westlake Education Foundation.

Author Contributions

D.M. conceived the project and wrote the manuscript. D.M. supervised on and provided methodology to structural and functional studies. X.W. supervised on and provide methodology to nanobody screening, validation and application. J.L. contributed to protein expression and purification, cryo-EM sample preparation, data collection, assay system set up and biochemical assays. J.S. contributed to cryo-EM data processing, model building,

purification of mutants and binding assay. A.S. contributed to nanobody screening, validation and purification. M.L. and M.X. contributed to homologues screening and assay system set up. K.Z. and P.L. performed ligands docking. G.H. contributed to cryo-EM data processing.

Ethics statement

Competing interests

The authors declare no competing interests.

Additional Information

Supplementary Information is available for this paper. Correspondence and requests for materials should be addressed to Dan Ma and Xudong Wu. Reprints and permissions information is available at www.nature.com/reprints.

Figure legends

Fig. 1 Structure of MPC in IMS-open conformation. a, Cryo-EM map of apo MPC in complex with Nb1 at pH 8.0. MPC1, MPC2, Nb1, PC/cardiolipin and other surrounding lipid-like densities are colored green, violet, grey, brown and light grey, respectively. This color scheme was used throughout the text. **b,** Overall structure of apo MPC in IMS-open conformation. Structure is shown in cartoon with MPC1 colored green, MPC2 colored violet, Nb1 colored grey, and the lipids colored brown. Key structural elements of both subunits are labeled in corresponding colors. Both side view and view from IMS side are shown. **c,** Electrostatic analysis result. A cut-away surface illustration of the structure shows a wide opening towards the IMS side. **d,** Interaction details between MPC1 and MPC2 on the matrix side. Hydrogen bonds are indicated as yellow dash lines in this and all following figures.

Fig. 2 Structure of pyruvate-treated MPC in occluded conformation. a, Cryo-EM map of pyruvate-treated MPC in complex with Nb1 at pH 6.8. **b,** Overall structure of pyruvate-treated MPC in complex with Nb1 at pH 6.8. **c,** A cut-away surface illustration of pyruvate-treated MPC purified at pH 6.8 suggests an occluded conformation. The putative pyruvate binding pocket is highlighted by a red square. **d,** Conservation of the residues forming the putative pyruvate binding pocket. Transparency of cartoon is set as 40%. The conservation surface was generated with the ConSurf web server. **e,** Comparison of pyruvate uptake by WT MPC and mutants carrying mutations in the putative pyruvate binding site. Proteoliposome-based transport assay using [^{14}C]-pyruvate was performed for 30 s followed by scintillation counting. Internal pH of liposomes was 8.0 and external pH was 6.4. Y axis represents relative pyruvate uptake with that of WT as 100%. In all assay figures, residues on MPC1 and MPC2 are colored green and violet, respectively. Average value of empty liposomes was used as control and

subtracted. **f,** 'Zipper'-like interactions between L1 loops on the IMS side. **g,** Comparison of pyruvate uptake by WT MPC and mutants carrying mutations on L1 loops. **h,** Interaction between MPC1 and MPC2 mediated by MPC2-Gln71, MPC2-Gln110 and other nearby residues. **i,** Comparison of pyruvate uptake by WT MPC and MPC2-Gln71, MPC2-Gln110 mutants. In all transport assay figures, data are shown as mean ± SD, n = 3 technical replicates. All transport assay experiments were independently repeated twice with similar results. For original data of all the assays in this study, see Source Data.

Fig. 3 Structure of UK5099-bound MPC. a, Cryo-EM map of MPC-Nb1 complex treated with UK5099. **b,** Overall structure of UK5099-bound MPC with the binding pocket highlighted in grey color. UK5099 is colored yellow. The pocket is generated via PyMOL by showing solid surface with cavities and pockets culled at 60% transparency. **c,** Interaction details between UK5099 and MPC. **d,** Comparison of substrate transport activity of WT MPC and the UK5099 binding site mutant MPC2-W82D. **e,** Comparison of UK5099 inhibition on substrate transport by WT MPC and UK5099 binding site mutant with control subtracted. For dose-dependent inhibition assay, proteoliposomes were pre-incubated with a series of UK5099 concentrations (0.001nM, 10 nM, 50 nM, 100 nM, 500 nM, 1 μM, 5 μM, 10 μM, 50 μM and 100 μM) for 1 min at room temperature before the reaction initiated by the addition of 50 μM [^{14}C]-pyruvate. The IC_{50} values were determined using nonlinear regression fittings in GraphPad Prism 10 [Inhibitor] vs. response -- Variable slope (four parameters)] with constrain settings of 'Bottom constant equal to 0, Top constant equal to 100'. In all transport assay figures, data are shown as mean ± SD, n = 3 technical replicates. All transport assay experiments were independently repeated twice with similar results.

Fig. 4 Structure of MPC in matrix-facing state with a nanobody block the transport path. a, Cryo-EM map of pyruvate-treated MPC in complex with Nb1 and Nb2, at pH 6.8. **b,** Overall structure of Nb1-MPC-Nb2 complex. **c,** A cut-away surface illustration of Nb1-MPC-Nb2 complex. **d,** Interaction details between Nb2 and MPC. **e,** Structural alignment between structures of MPC in Nb1-MPC-Nb2 and UK5099-bound complexes. Pocket-forming residues on the matrix side of the two structures are highlighted. **f,** Comparison between the binding pattern between MPC and the two inhibitory molecules. Only conserved polar interactions with MPC1-Tyr62 and MPC2-Lys49 are shown.

Fig. 5 Conformational changes of MPC. a, Structural alignment between TMDs of MPC in the occluded structure and the IMS-open structure. **b,** Superimposition of TMDs of corresponding subunits from the IMS-open structure and the occluded structure. **c,** Superimposition of structures in the occluded state and the matrix-facing state (Nb2-bound). Structural elements are labeled in green and violet numbers for MPC1 and MPC2, respectively. **d,** Comparison of the gating residues on the matrix side between the occluded state and the matrix-facing state. **e,** Comparison of the putative pyruvate binding site in the structures of MPC in IMS-open, occluded and matrix-facing states. The putative binding site are indicated by MPC2-Lys49 in the cutting-surface illustration of the three structures.

Extended data figure legends

Extended Data Fig. 1 | Cryo-EM samples preparation and validation. a, Time course profile for pyruvate transport by purified WT MPC. Black dots represent readings for proteoliposomes incorporated with MPC and black squares represent readings for empty liposomes. Internal pH was 8.0

and external pH was 6.4. In the following transport assay experiments we chose to measure pyruvate uptake by MPC at the time point of 30 s, which is approximately within the linear range. **b,** Influence of different termination conditions on substrate transport. In the following transport assay experiments we added 1 mM of UK5099 for transport termination. **c,** K_m value determination for WT MPC. The K_m value was obtained from automatic curve fitting within the pyruvate concentration range of 100-600 μM. **d,** Transport activity of WT MPC with or without binding to nanobodies. MPC samples were pre-incubated with corresponding nanobodies before incorporated into liposomes. Liposomes were run into SDS-PAGE to monitor incorporation efficiency of different MPC samples. **e,** Protein complexes purified for cryo-EM analyses. Peak containing desired complex in each gel filtration profile is indicated by a red star, and peak fractions were analyzed by SDS-PAGE. Each MPC sample was purified at least twice with similar behavior. For all gels, the same molecular weight marker was used as that in panel **d**, and for uncropped gels, see Supplementary Figure 1. In all transport assay figures, data are shown as mean ± SD, n = 3 technical replicates. All transport assay experiments were independently repeated twice with similar results.

Extended Data Fig. 2 | Cryo-EM analysis of MPC in IMS-open state. a, Cryo-EM analysis of apo MPC in complex with Nb1 at pH 8.0. **b,** Cryo-EM analysis of apo MPC in complex with Nb1 at pH 6.8. **c,** Cryo-EM analysis of pyruvate-treated MPC in complex with Nb1 at pH 8.0. For each sample, a representative raw micrograph, 2D-class averages of particle images, the flowchart of the EM analysis, the local resolution map, the angular distribution of the particles, the Fourier shell correlation (FSC) curve and the FSC curve of the refined model versus the corresponding map in MPC region are shown.

Extended Data Fig. 3 | Cryo-EM analysis of MPC in occluded state and matrix-facing state. a, Cryo-EM analysis of pyruvate-treated MPC in complex with Nb1 at pH 6.8. **b,** Cryo-EM analysis of UK5099-bound MPC in complex with Nb1. **C,** Cryo-EM analysis of pyruvate-treated MPC in complex with Nb1 and Nb2 at pH 6.8. For each sample, a representative raw micrograph, 2D-class averages of particle images, the flowchart of the EM analysis, the local resolution map, the angular distribution of the particles, the Fourier shell correlation (FSC) curve and the FSC curve of the refined model versus the corresponding map in MPC region are shown.

Extended Data Fig. 4 | Structural features of MPC structures in IMS-open state. a, Overall structures of MPC purified in different conditions that exhibit IMS-open conformation. **b,** Structural alignment of the three MPC structures in IMS-open state. **c,** Superimposition of TMDs of MPC1 and MPC2. **d,** Structure details of MPC2-APH. **e,** Density for the cardiolipin molecule found between MPC2-APH and MPC1-TMD. **f,** Density for the PC molecule found between MPC1-TM1 and MPC2-TM2. All figures of local densities were generated by isomesh function in PyMOL at sigma value of 4.5.

Extended Data Fig. 5 | Importance of structural features in the occluded MPC structure. a, Cryo-EM densities of residues forming the putative pyruvate binding pocket in the occluded MPC structure. **b,** Gel filtration profiles of corresponding MPC variants. Peak positions of MPC are indicated by reverse triangles. The differences in elution volume of MPC variants are mainly due to different equipment and columns were used during purification. Each MPC mutant was purified at least twice with similar

behavior. **c,** Substrate transport by MPC carrying mutations on residues in the putative pyruvate binding pocket. **d,** Time courses of pyruvate transport by putative pyruvate binding pocket mutants. **e,** Cryo-EM densities of the L1 loops in the occluded structure. **f,** Substrate transport by MPC carrying mutations on residues in the L1 loops. **g,** Cryo-EM densities of residues mediating interaction between MPC1 and MPC2 below the L1 loops on the IMS side of the occluded structure. **h,** Substrate transport by MPC carrying MPC2-Q71A, Q110A and Q110H mutations. For all gels, the same molecular weight marker was used as that in panel **c**, and for uncropped gels, see Supplementary Figure 1. In all transport assay figures, data are shown as mean ± SD, n = 3 technical replicates. All transport assay experiments were independently repeated twice with similar results.

Extended Data Fig. 6 | Binding features of inhibitors towards MPC. a, Chemical structure of UK5099. Key structural elements of UK5099 discussed in main text are indicated. **b,** Densities of UK5099 and binding pocket forming residues. All densities are isolated at sigma value of 4.5. **c,** Gel filtration profiles of WT MPC and the mutant carrying MPC2-W82D mutation. The mutant was purified at least twice with similar behavior. **d,** Microscale thermophoresis (MST) binding measurement of MPC variants towards UK5099 at different maximum UK5099 concentrations. Binding curves of MPC variants are presented. Binding affinity between WT and UK5099 is 353.8 ± 97.03 nM, while binding between binding pocket mutants and UK5099 was not detectable in the UK5099 concentration range of up to 2 μM. Binding affinities between the mutants and UK5099 could be detected at 159.2 ± 26.72 μM for K49A mutant, 122.8 ± 20.57 μM for W82A mutant, 269.1± 15.40 μM for W82D mutant and 122.4 ± 22.99 μM for N100A mutant, respectively, in the UK5099 concentration range of up to 300 μM. Error bars represent mean ± SD based on three independent measurements. **e,** Substrate transport of WT MPC and the mutant carrying MPC2-W82D mutation. Data are shown as mean ± SD, n = 3 technical replicates. Experiments were independently repeated twice with similar results. For uncropped gel, see Supplementary Figure 1. **f,** Ligand docking results of known inhibitors towards MPC. General fitting of inhibitors in the UK5099 binding pocket in the overall structure context of MPC. **g,** In silico docking results of known inhibitors targeting the UK5099 binding pocket. Ligands are shown in the UK5099 binding pocket (grey, 60% transparency).

Extended Data Fig. 7 | Cryo-EM densities of the putative gating residues on the matrix side. Densities for corresponding residues in the occluded structure and the Nb2-bound matrix-facing structure are shown.

Extended Data Fig. 8 | Sequence alignments of MPC subunits among different species. a, Sequence alignment of MPC1. Sequences were obtained from UniProt with the following accession codes of MPC1 from corresponding species: *Homo sapiens* (Q9Y5U8), *Mus musculus* (P63030), *S. cerevisiae* (P53157), *C. elegans* (Q21828), *D. melanogaster* (Q7KSC4) and *Danio rerio* (F1Q6Z3). **b,** Sequence alignment of MPC2 from different species and MPC3 from *S. cerevisiae*. Sequences were obtained from UniProt with the following accession codes of MPC2 from corresponding species: *Homo sapiens* (O95563), *Mus musculus* (Q9D023), *S. cerevisiae* (P38857), *C. elegans* (O01578), *D. melanogaster* (Q9VHB2), *Danio rerio* (Q7ZUJ3) and MPC3 from *S. cerevisiae* (P53311). In the sequence alignment results in panels **a** and **b**, residues forming the putative pyruvate binding pocket in

the occluded structure are indicated by reversed blue triangles, zipper-forming residues on L1 loops are indicated by reversed red triangles, residues mediating interactions between MPC1 and MPC2 below L1 loops are indicated by green squares, and UK5099 binding pocket forming residues are indicated by red dots. **c,** Difference in UK5099 binding pocket between human MPC and yeast MPC. Pockets were generated using PyMOL. The pocket of yeast MPC was mimicked by mutating corresponding residues in our UK5099-bound cryo-EM structure model. The opening of each binding pocket is highlighted by a red dashed line.

Extended Data Fig. 9 | Structural comparison between structures of MPC and SemiSWEETs. a, Structural comparison between the IMS-open MPC and an inward-open (cytoplasm-facing) SemiSWEET (PDB code: 4X5M). **b,** Structural comparison between occluded structure of MPC and structures of SemiSWEETs (PDB code: 4RNG and 4QNC) in occluded conformation. **c,** Structural comparison between the matrix-facing MPC and an outward-open SemiSWEET (PDB code: 4QND). **d,** The putative substrate binding pocket in SemiSWEET. An occluded structure of SemiSWEET (PDB code: 4RNG) was used for the cut-away surface generation. **e,** Comparison between the putative substrate binding pocket forming residues in occluded structures of MPC and SemiSWEET.

Extended Data Table 1 | Cryo-EM data collection, refinement and validation statistics.

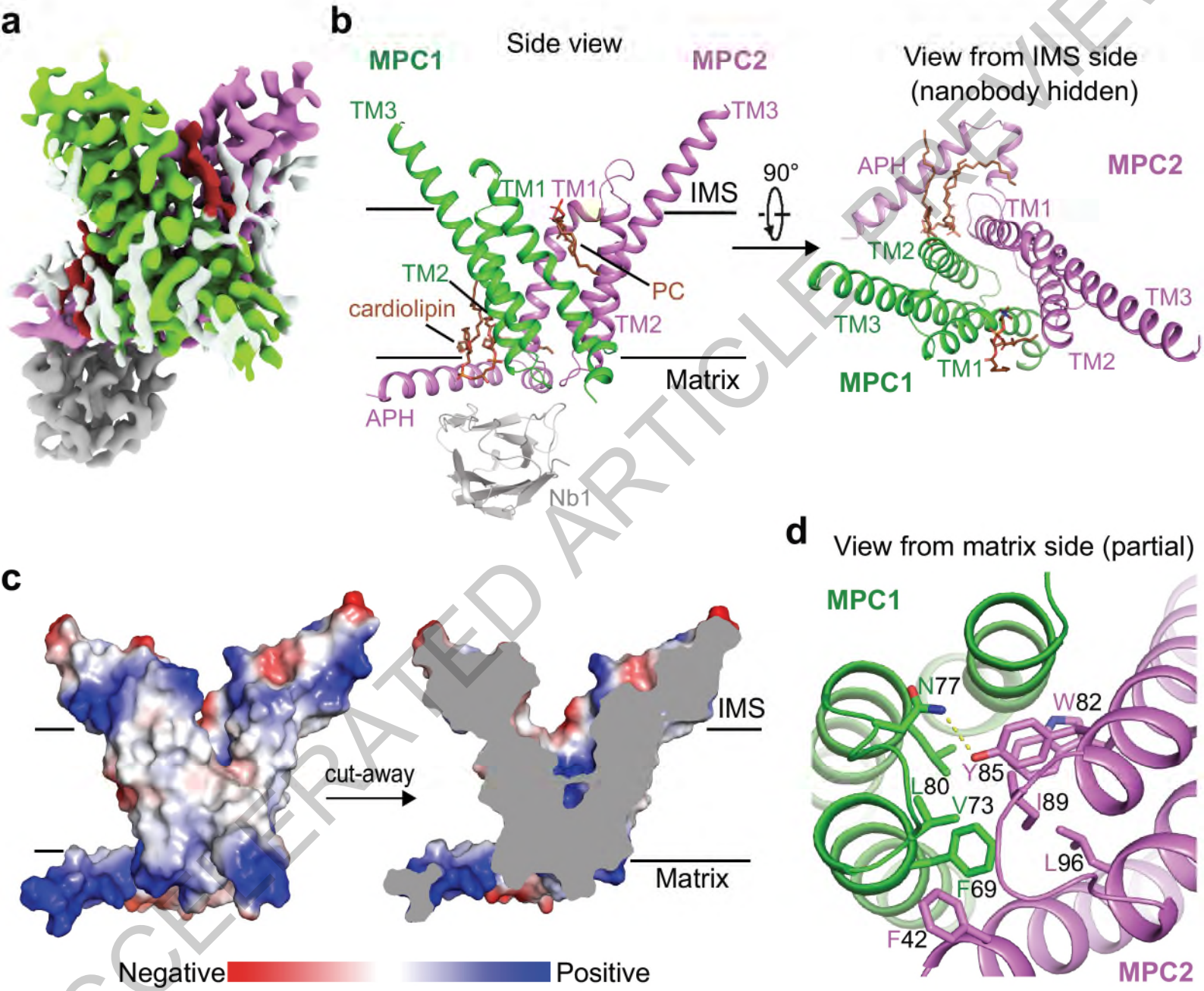

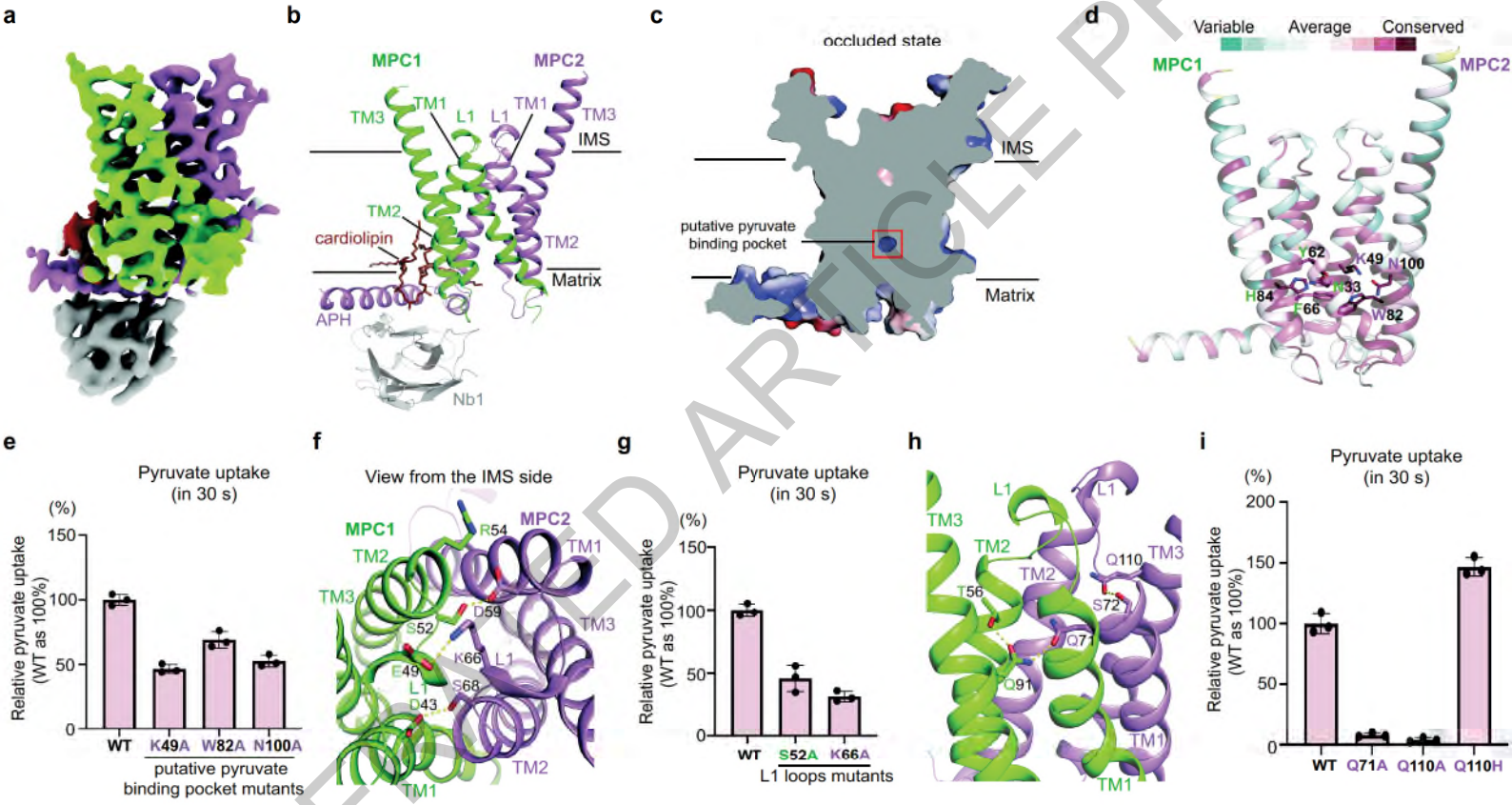

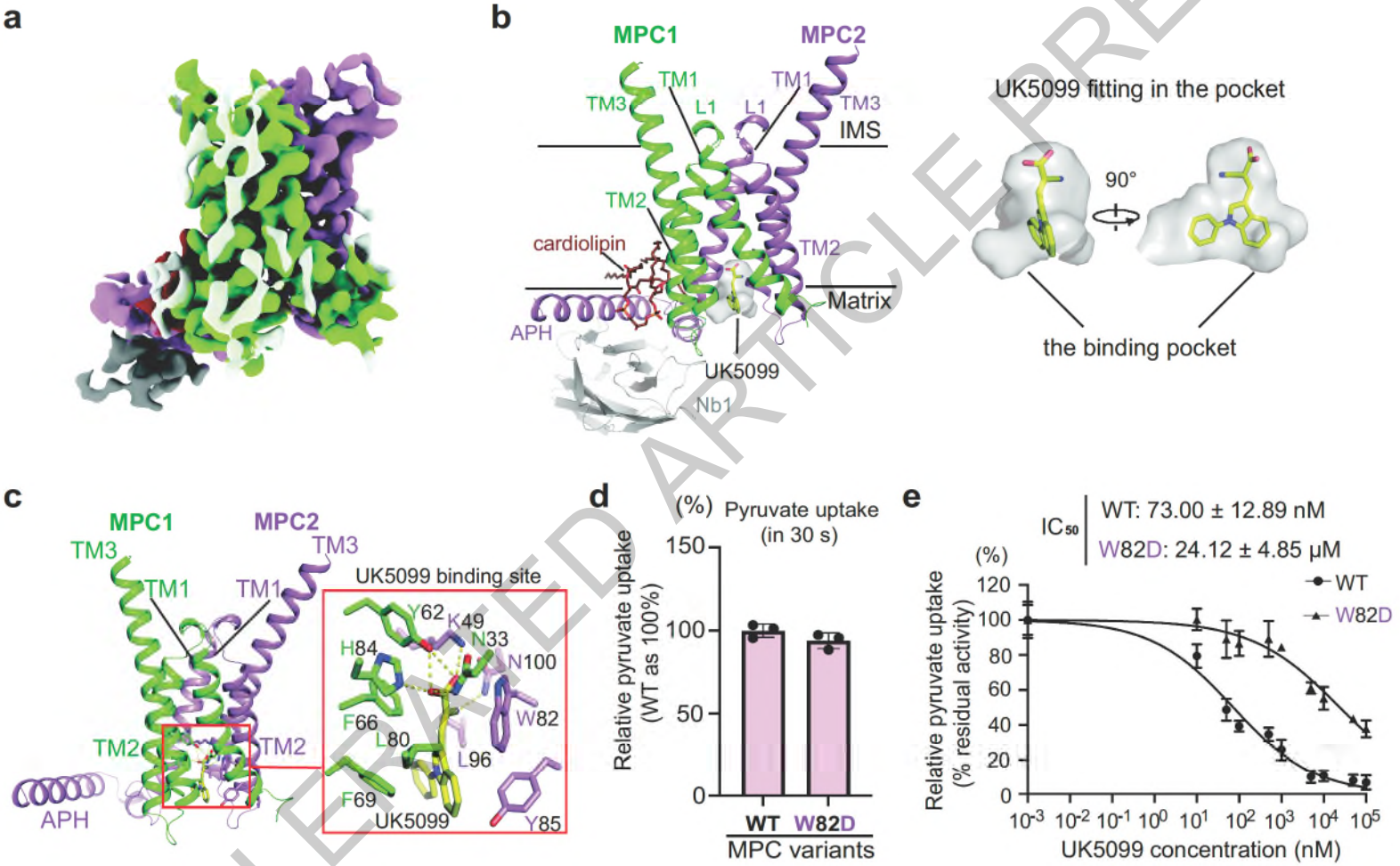

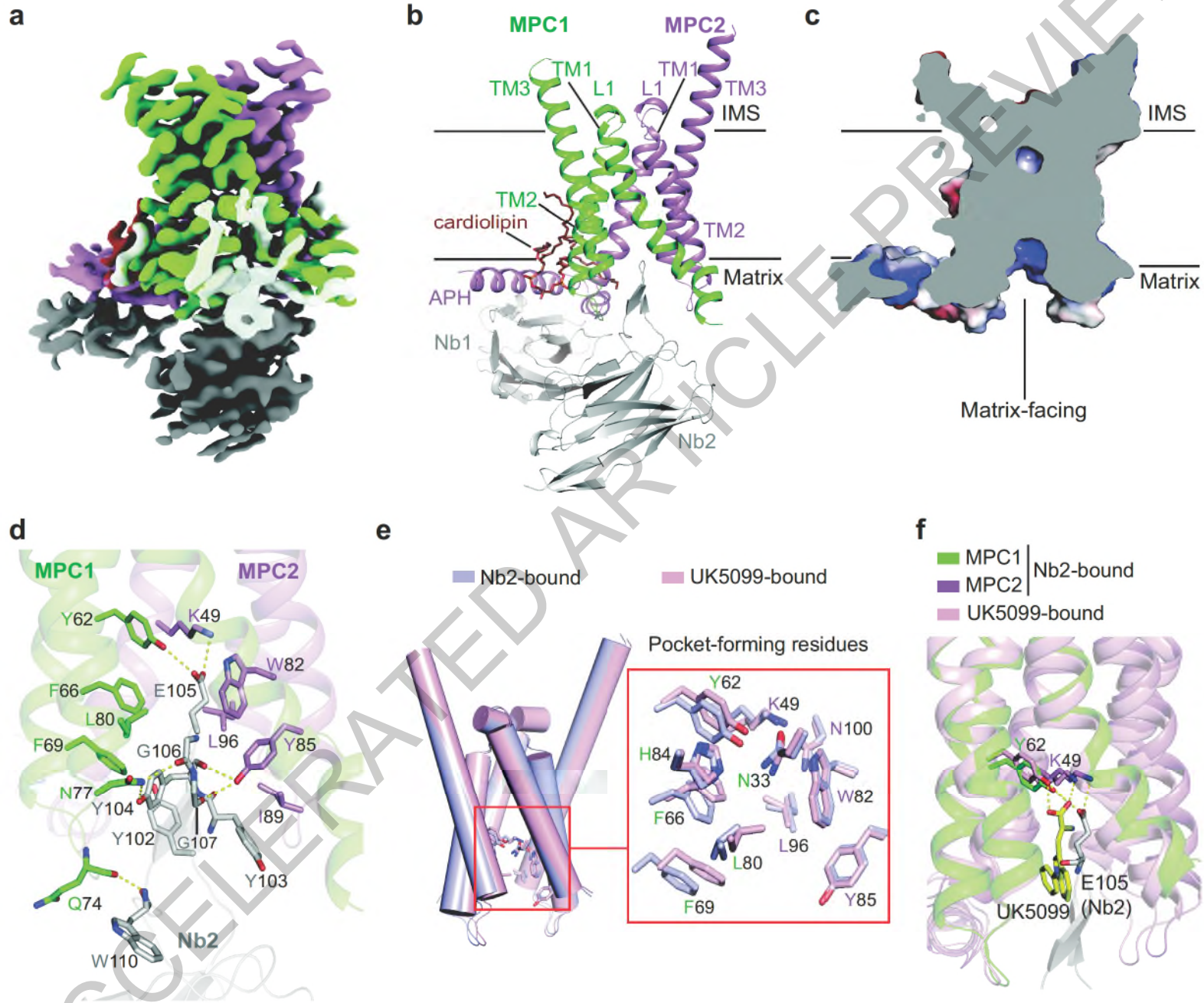

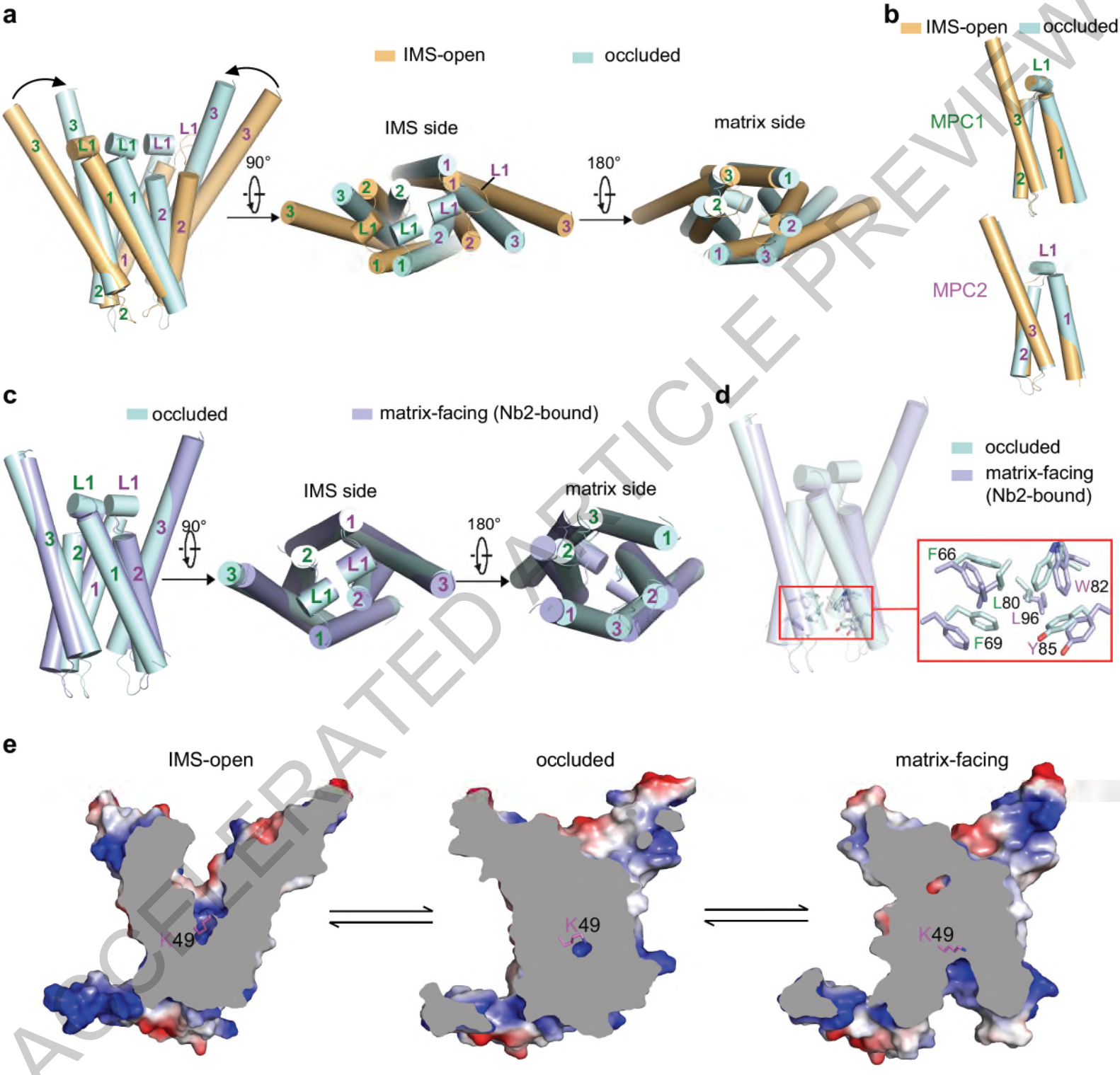

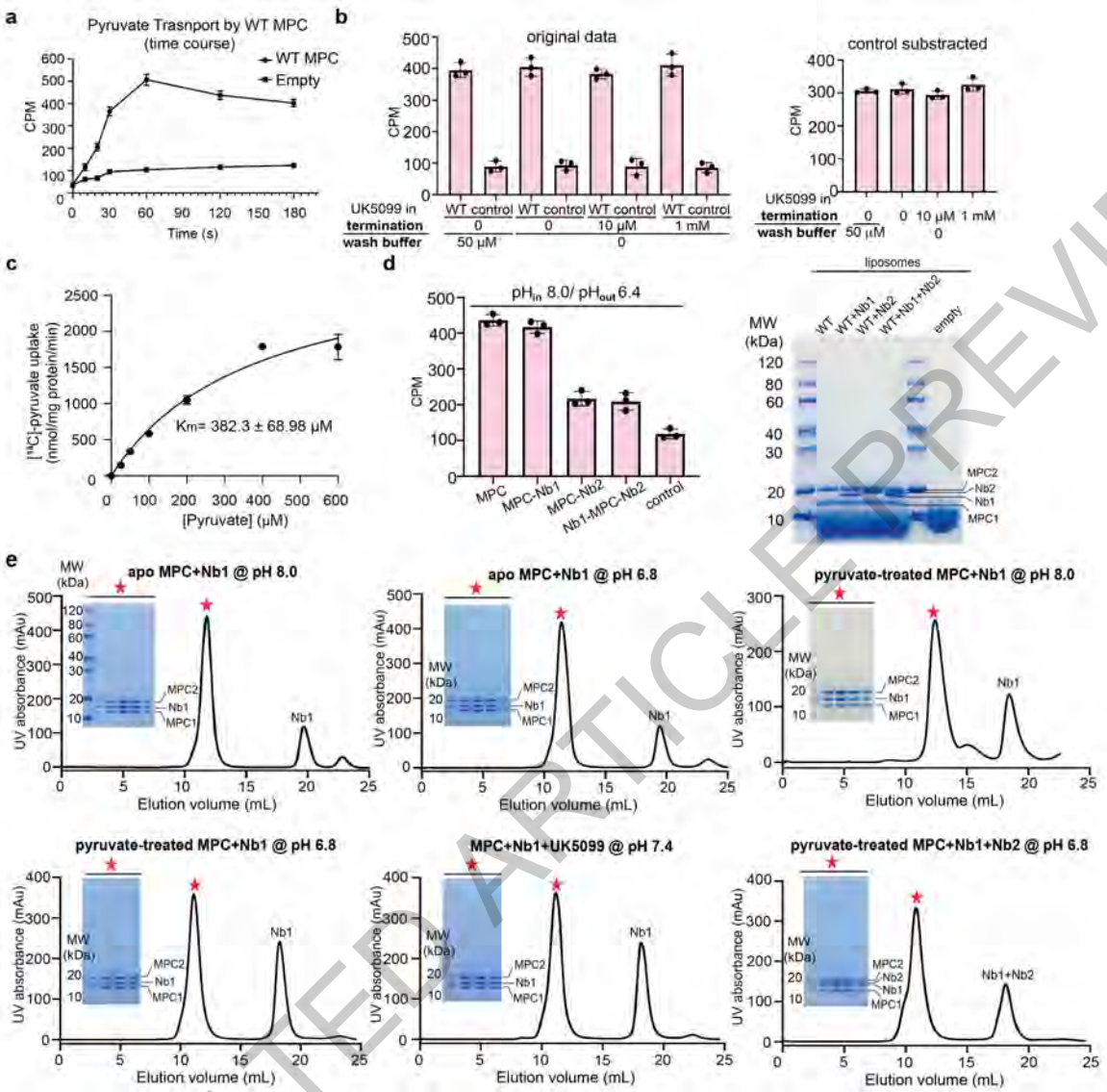

Extended Data Fig. 1

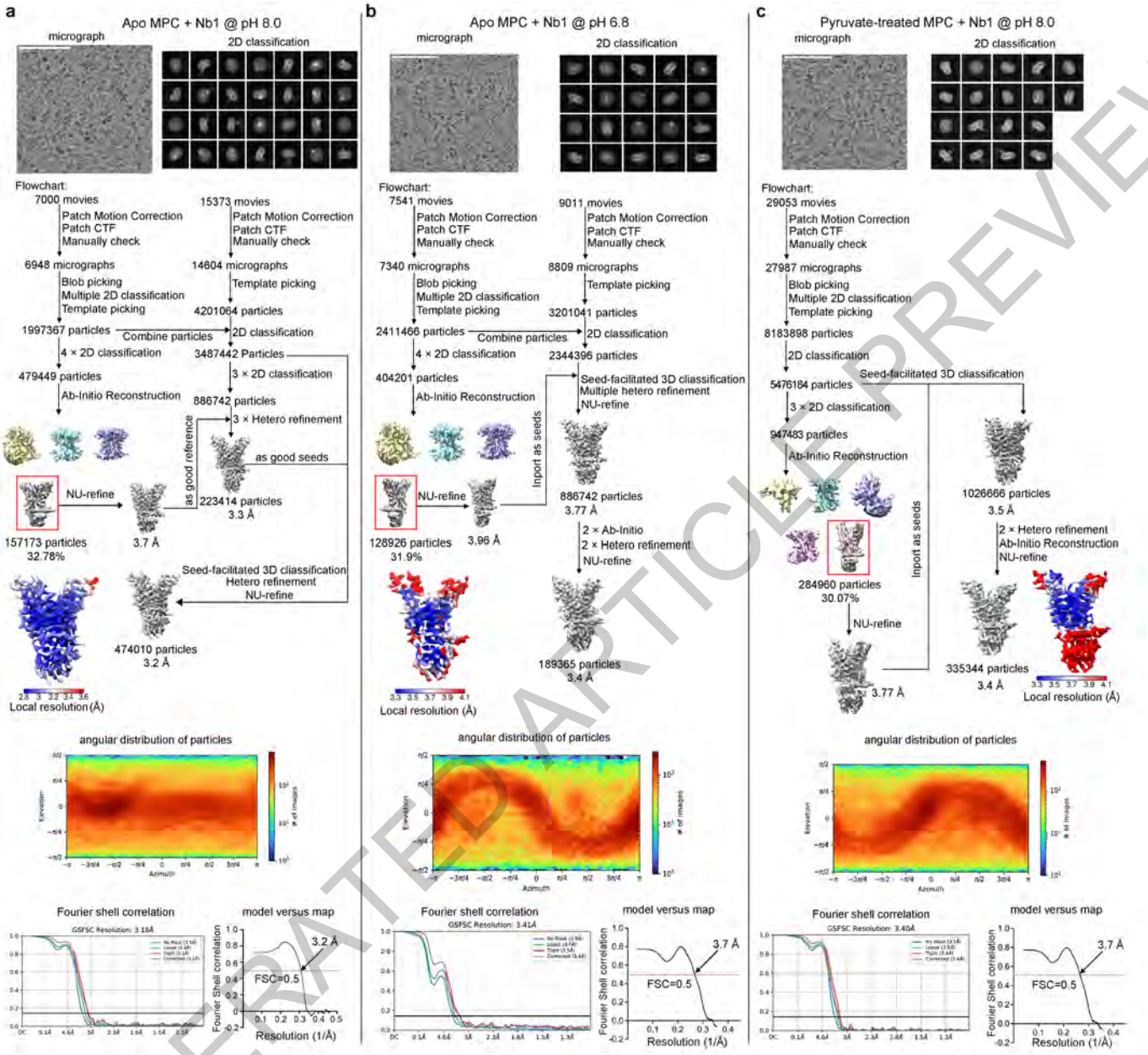

Extended Data Fig. 2

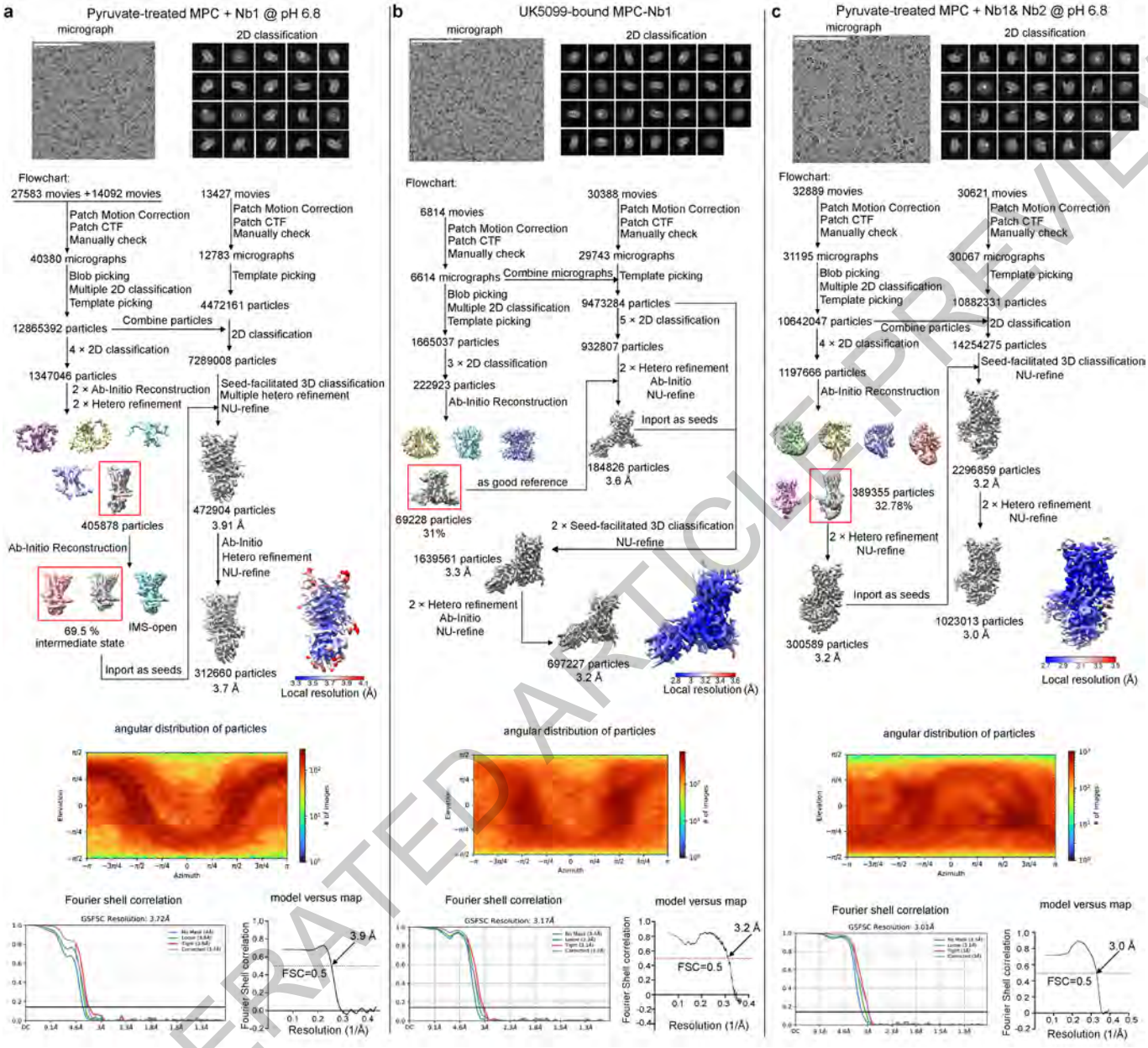

Extended Data Fig. 3

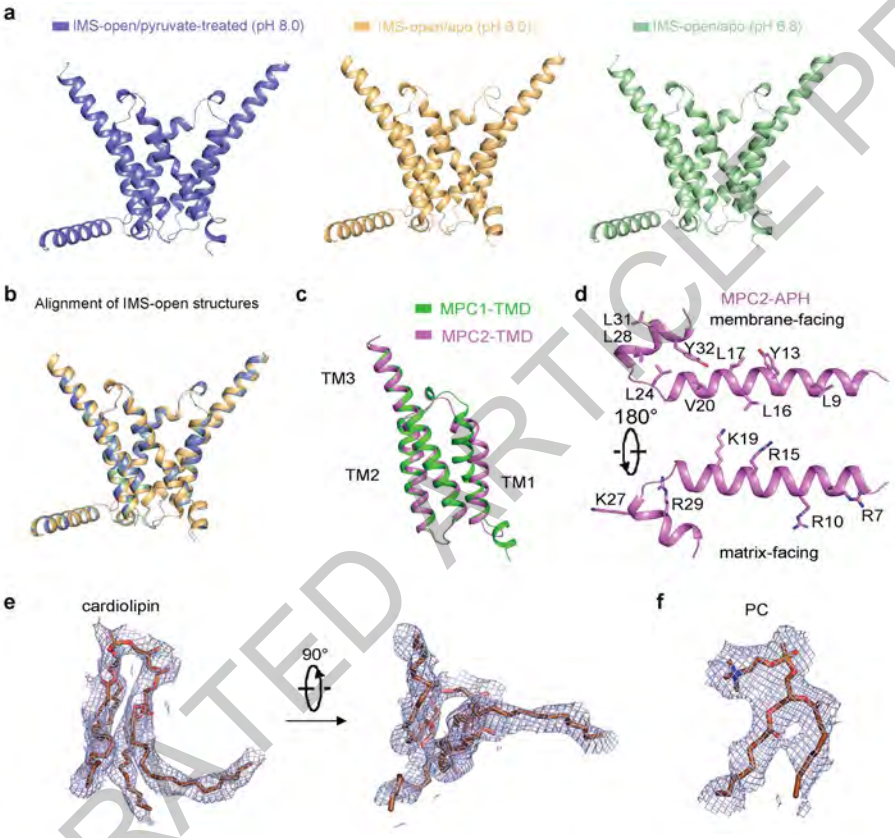

Extended Data Fig. 4

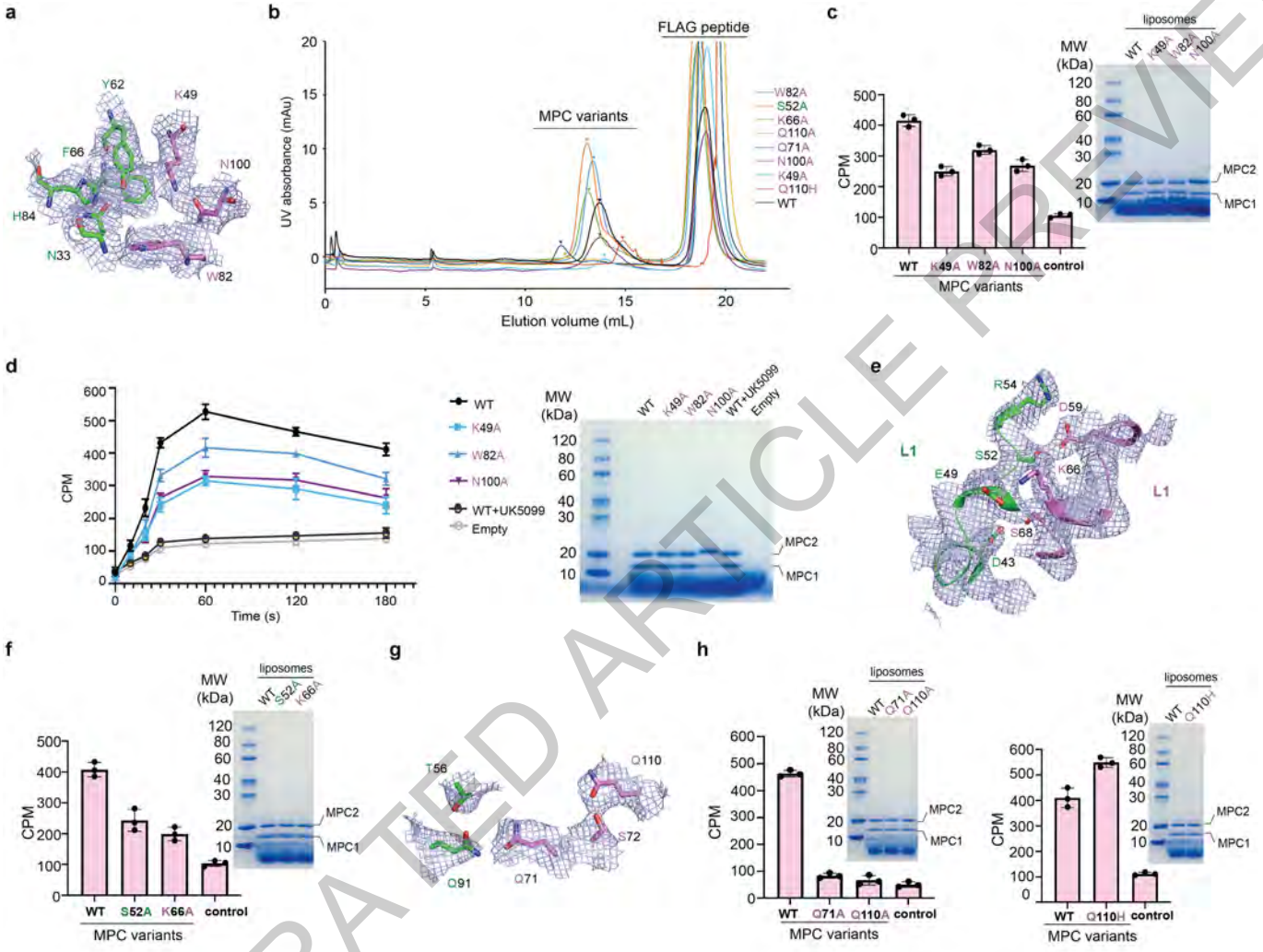

Extended Data Fig. 5

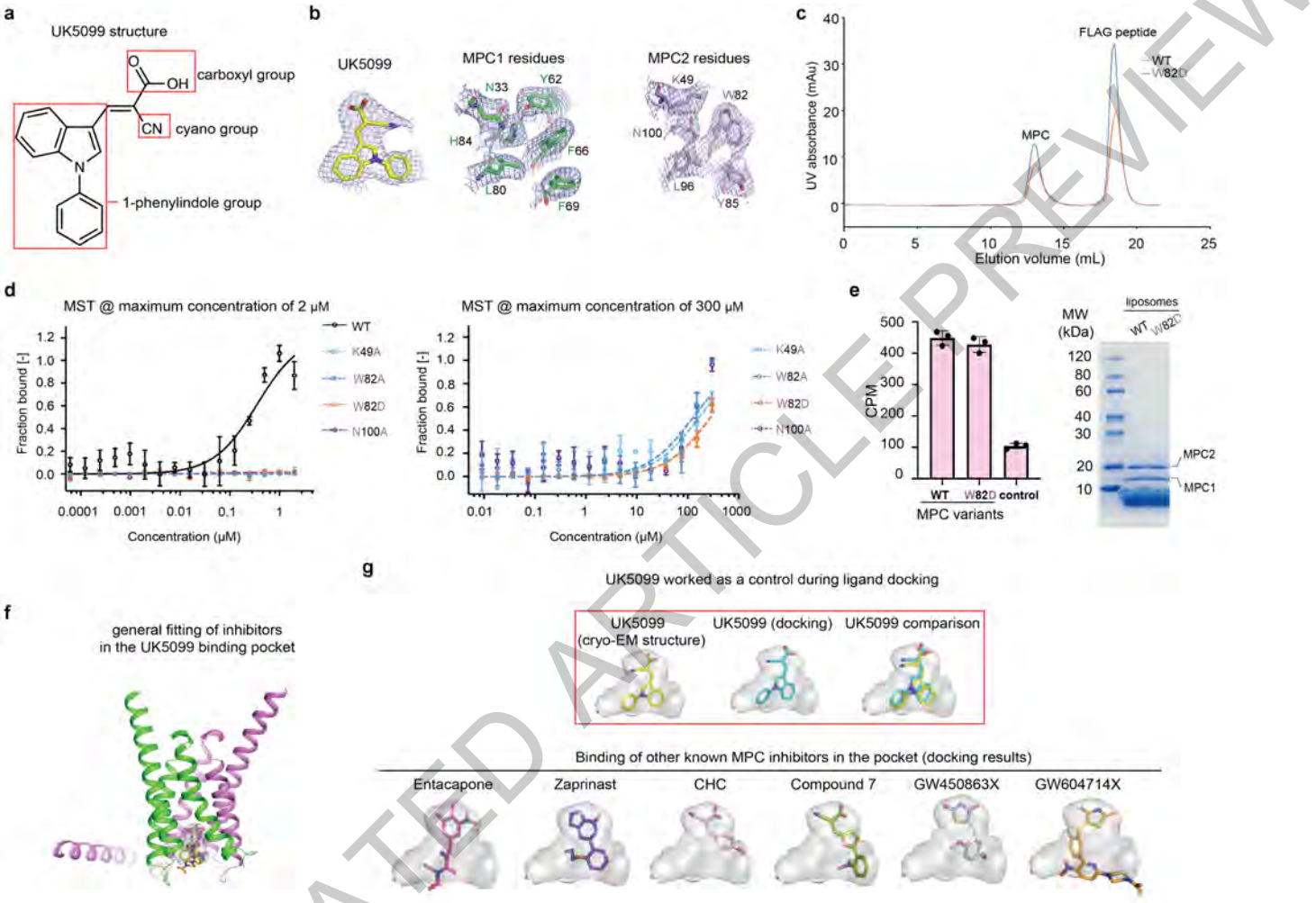

Extended Data Fig. 6

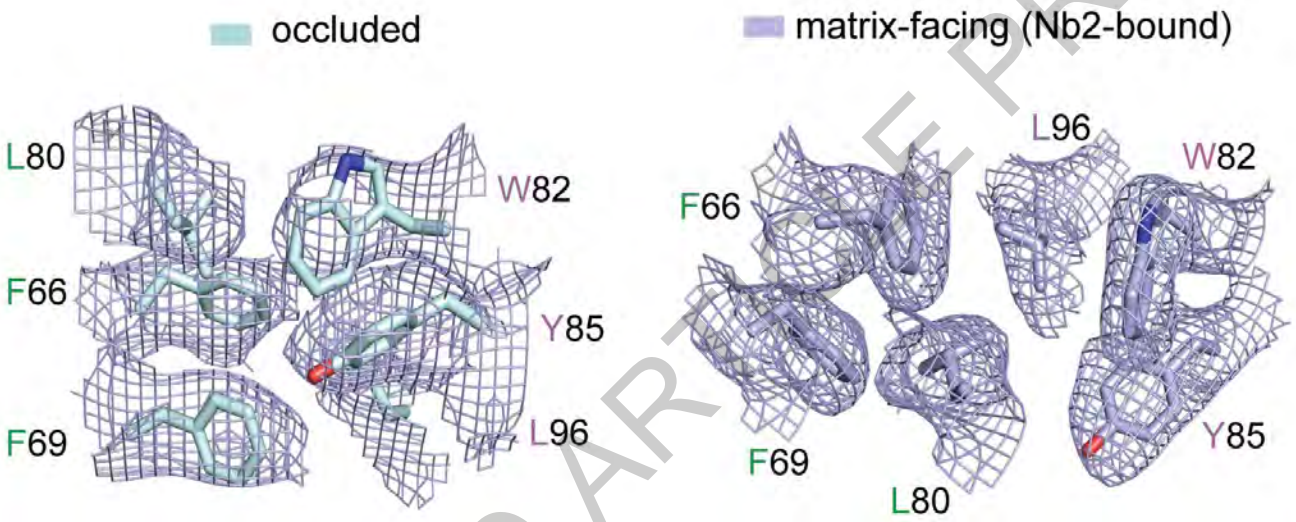

Extended Data Fig. 7

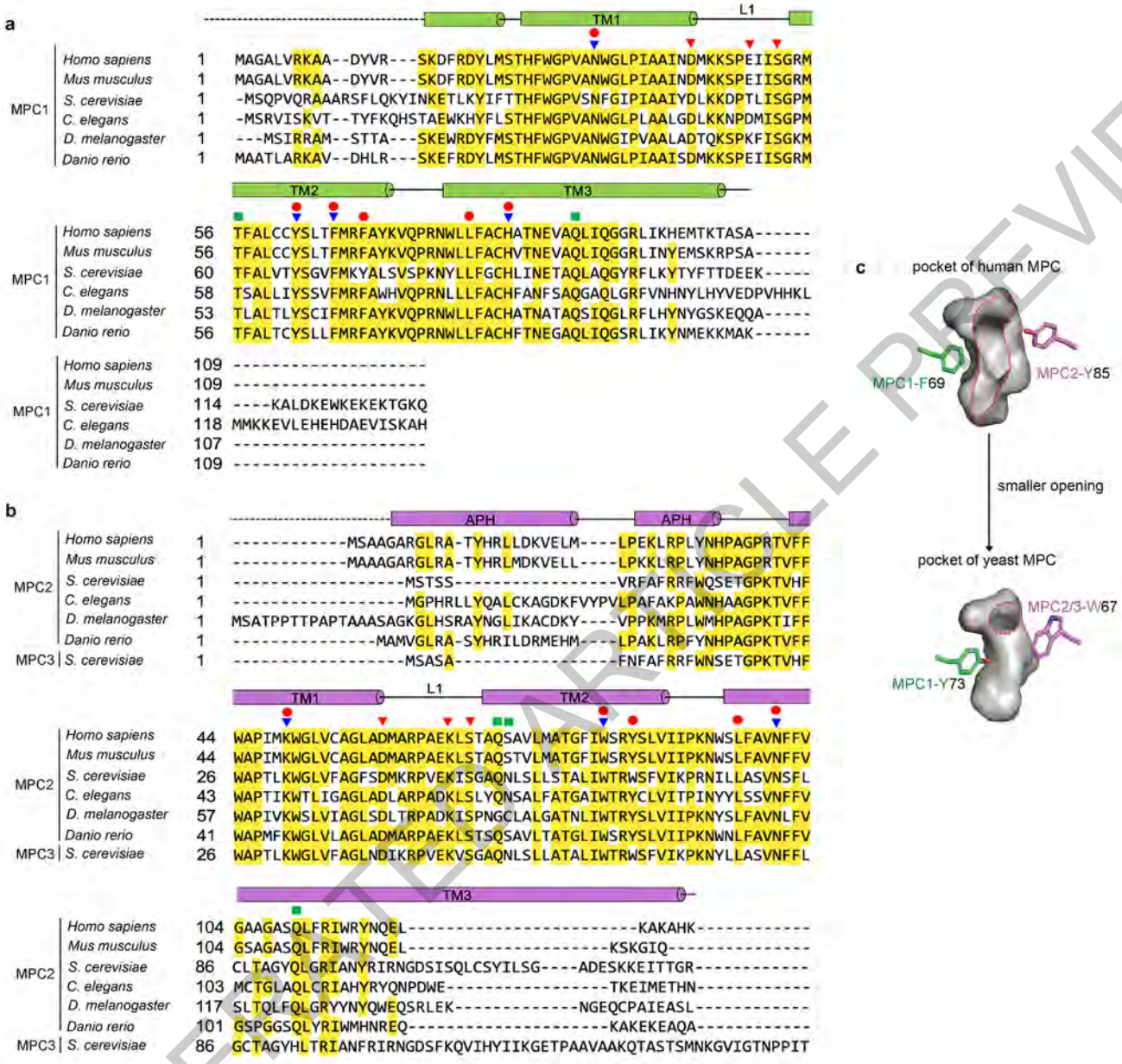

Extended Data Fig. 8

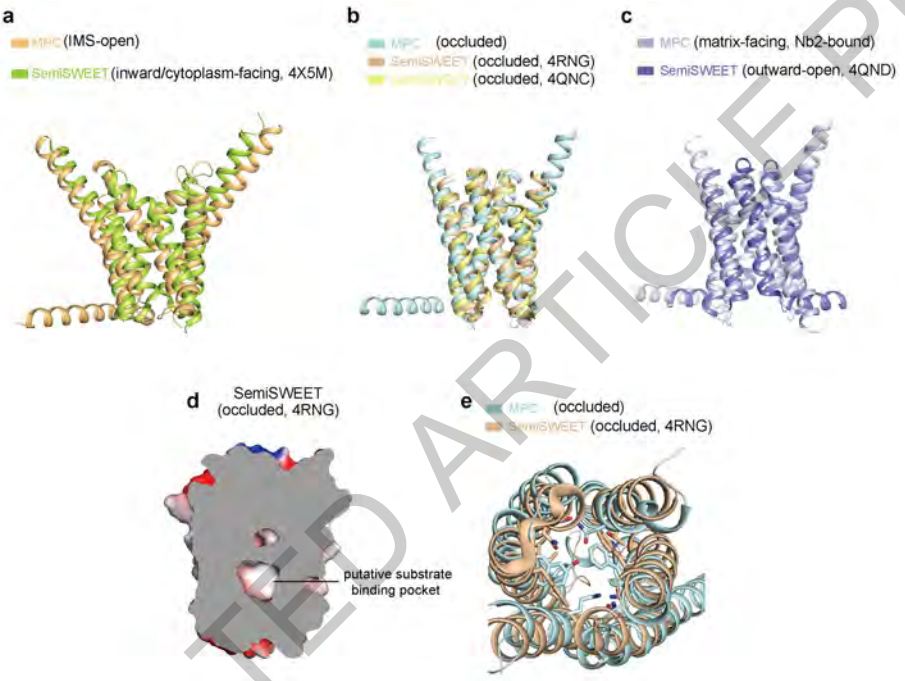

Extended Data Fig. 9

	apo MPC+ Nb1 pH 8.0 IMS-open (EMDB-39624) (PDB 8YW6)	apo MPC+ Nb1 pH 6.8 IMS-open (EMD-62464) (PDB 9KNW)	pyruvate-treated MPC + Nb1 pH 8.0 IMS-open (EMD-62466) (PDB 9KNY)	pyruvate-treated MPC + Nb1 pH 6.8 occluded (EMD-62465) (PDB 9KNX)	UK5099-bound MPC + Nb1 pH 7.4 matrix-facing (EMDB-39625) (PDB 8YW8)	pyruvate-treated MPC+Nb1&Nb2 pH 6.8 matrix-facing (EMDB-39626) (PDB 8YW9)
Data collection and processing						
Magnification	12500	12500	12500	12500	12500	12500
Voltage (kV)	300	300	300	300	300	300
Electron exposure ($e^-/Å^2$)	50	50	50	50	50	50
Defocus range (μm)	-0.8~-1.2	-0.8~-1.2	-0.8~-1.2	-0.8~-1.2	-0.8~-1.2	-0.8~-1.2
Pixel size (Å)	0.57	0.57	0.57	0.57	0.57	0.57
Symmetry imposed	*C1*	*C1*	*C1*	*C1*	*C1*	*C1*
Initial particle images (no.)	6,198,431	5,612,507	8,183,898	17,337,553	9,473,284	21,524,378
Final particle images (no.)	474,010	189,365	335,344	312,660	697,227	1,023,013
Map resolution (Å)	3.18	3.41	3.40	3.72	3.17	3.01
FSC threshold	0.143	0.143	0.143	0.143	0.143	0.143
Map resolution range (Å)	1.19 ~ 10.46	1.19 ~ 12.15	1.19 ~ 10.95	1.18 ~ 9.75	2.73 ~ 9.66	1.78 ~ 8.64
Refinement						
Initial model used	Predicted	Predicted	Predicted	Predicted	Predicted	Predicted
Model resolution (Å)	3.3	3.7	3.7	3.9	3.2	3.1
FSC threshold	0.5	0.5	0.5	0.5	0.5	0.5
Map sharpening *B* factor ($Å^2$)	-148.5	-136.7	-154.7	-222.1	-181.0	-169.8
Model composition						
Non-hydrogen atoms	2749	2749	2749	2677	2699	3711
Protein residues	333	333	333	329	329	458
Ligands	2	2	2	1	2	1
B factors ($Å^2$)						
Protein	71.99	69.06	69.06	64.34	38.05	60.52
Ligand	20.00	57.00	57.00	48.70	21.88	20.45
R.m.s. deviations						
Bond lengths (Å)	0.009 (0)	0.004 (0)	0.004 (0)	0.008 (0)	0.009 (0)	0.007 (0)
Bond angles (°)	1.053 (0)	0.656 (0)	0.640 (0)	0.917 (0)	1.192 (0)	0.833 (0)
Validation						
MolProbity score	0.57	1.77	2.14	1.57	1.03	1.52
Clashscore	0.18	12.52	11.60	8.45	2.43	6.00
Poor rotamers (%)	0.74	1.48	4.44	0.38	0.00	0.81
Ramachandran plot						
Favored (%)	99.39	97.86	97.86	96.28	99.07	96.89
Allowed (%)	0.61	2.14	2.14	3.72	0.93	3.11
Disallowed (%)	0.00	0.00	0.00	0.00	0.00	0.00

Extended Data Table 1

nature portfolio

Corresponding author(s): Dan Ma; Xudong Wu

Last updated by author(s): 2025-02-28

Reporting Summary

Nature Portfolio wishes to improve the reproducibility of the work that we publish. This form provides structure for consistency and transparency in reporting. For further information on Nature Portfolio policies, see our Editorial Policies and the Editorial Policy Checklist.

Please do not complete any field with "not applicable" or n/a. Refer to the help text for what text to use if an item is not relevant to your study.
For final submission: please carefully check your responses for accuracy; you will not be able to make changes later.

Statistics

For all statistical analyses, confirm that the following items are present in the figure legend, table legend, main text, or Methods section.

n/a	Confirmed	
☐	☒	The exact sample size (*n*) for each experimental group/condition, given as a discrete number and unit of measurement
☐	☒	A statement on whether measurements were taken from distinct samples or whether the same sample was measured repeatedly
☒	☐	The statistical test(s) used AND whether they are one- or two-sided *Only common tests should be described solely by name; describe more complex techniques in the Methods section.*
☒	☐	A description of all covariates tested
☒	☐	A description of any assumptions or corrections, such as tests of normality and adjustment for multiple comparisons
☐	☒	A full description of the statistical parameters including central tendency (e.g. means) or other basic estimates (e.g. regression coefficient) AND variation (e.g. standard deviation) or associated estimates of uncertainty (e.g. confidence intervals)
☒	☐	For null hypothesis testing, the test statistic (e.g. *F*, *t*, *r*) with confidence intervals, effect sizes, degrees of freedom and *P* value noted *Give P values as exact values whenever suitable.*
☒	☐	For Bayesian analysis, information on the choice of priors and Markov chain Monte Carlo settings
☒	☐	For hierarchical and complex designs, identification of the appropriate level for tests and full reporting of outcomes
☒	☐	Estimates of effect sizes (e.g. Cohen's *d*, Pearson's *r*), indicating how they were calculated

Our web collection on statistics for biologists contains articles on many of the points above.

Software and code

Policy information about availability of computer code

Data collection	EPU-3.4.0.5704REL
Data analysis	cryoSPARC-4.4.1, UCSF Chimera-1.16, ChimeraX-1.3, PHENIX-1.19.1-4122, Coot-0.9.2, Pymol-2.5.4, AlphaFold2, Graphpad Prism 10.2.1, ADFR suite v1.0, AutoGrid v4.2.7, OpenBabel v3.1.0, Meeko v0.5.1, AutoDock-Vina v1.2.5, ConSurf Web Server

For manuscripts utilizing custom algorithms or software that are central to the research but not yet described in published literature, software must be made available to editors and reviewers. We strongly encourage code deposition in a community repository (e.g. GitHub). See the Nature Portfolio guidelines for submitting code & software for further information.

Data

Policy information about availability of data

All manuscripts must include a data availability statement. This statement should provide the following information, where applicable:

- Accession codes, unique identifiers, or web links for publicly available datasets
- A description of any restrictions on data availability
- For clinical datasets or third party data, please ensure that the statement adheres to our policy

Atomic coordinates and corresponding EM maps of the structures of apo MPC in complex with Nb1 at pH 8.0 (PDB ID: 8YW6 and EMDB ID: EMD-39624) and pH 6.8 (PDB ID: 9KNW and EMDB ID: EMD-62464) in IMS-open state, structure of pyruvate-treated MPC in complex with Nb1 at pH 8.0 in IMS-open state (PDB ID: 9KNY and EMDB ID: EMD-62466), structure of pyruvate-treated MPC in complex with Nb1 at pH 6.8 in occluded state (PDB ID: 9KNX and EMDB ID: EMD-62465), structure of pyruvate-treated MPC in complex with Nb1 and Nb2 at pH 6.8 in matrix-facing/inhibitory state (PDB ID : 8YW9 and EMDB ID : EMD-39626), and UK5099-bound structure (PDB ID : 8YW8 and EMDB ID : EMD-39625) have been deposited in the Protein Data Bank (http://www.rcsb.org) and the Electron Microscopy Data Bank (https://www.ebi.ac.uk/pdbe/emdb/), respectively. The SemiSWEET structures used for structural comparisons with MPC in Extended Data Fig. 9 are accessible in the Protein Data Bank with PDB codes of 4X5M, 4RNG, 4QNC and 4QND.

Please select the one below that is the best fit for your research. If you are not sure, read the appropriate sections before making your selection.

☒ Life sciences ☐ Behavioural & social sciences ☐ Ecological, evolutionary & environmental sciences

For a reference copy of the document with all sections, see nature.com/documents/nr-reporting-summary-flat.pdf

Life sciences study design

All studies must disclose on these points even when the disclosure is negative.

Sample size	No predetermination of sample size. Sufficient cryo-EM data were collected to achieve adequate map resolutions. The sample sizes for all functional assay were chosen to ensure the reproducibility.
Data exclusions	Cryo-EM micrographs with ice or ethane contamination, empty holes, imaging of carbon support, and poor CTF fit (> 6 Å) were excluded manually. Particles belonging to bad classes were discarded and the data processing flowchart were summarized in Extended Data Figures. Above exclusions were based on well-established criteria.
Replication	Transport assays were independently repeated at least 2 times with three replicates each time, and binding assays were independently repeated for three times. All attempts at replication were successful with similar results.
Randomization	N/A. No clinical trials were involved, and no other large dataset was involved besides cryo-EM data, which were processed according to well-established criteria. For assays, due to enough control and good reproducibility, our results were sufficient to demonstrate the accuracy.
Blinding	N/A. No clinical trials were involved, and no other large dataset was involved besides cryo-EM data, which were processed according to well-established criteria. For assays, due to enough control and good reproducibility, our results were sufficient to demonstrate the accuracy.

Reporting for specific materials, systems and methods

We require information from authors about some types of materials, experimental systems and methods used in many studies. Here, indicate whether each material, system or method listed is relevant to your study. If you are not sure if a list item applies to your research, read the appropriate section before selecting a response.

Materials & experimental systems

n/a	Involved in the study
☐	☒ Antibodies
☐	☒ Eukaryotic cell lines
☒	☐ Palaeontology and archaeology
☒	☐ Animals and other organisms
☒	☐ Clinical data
☒	☐ Dual use research of concern
☒	☐ Plants

Methods

n/a	Involved in the study
☒	☐ ChIP-seq
☒	☐ Flow cytometry
☒	☐ MRI-based neuroimaging

Antibodies

Antibodies used	Two nanobodies used in this study were obtained through phage display, and named as Nb1 and Nb2 respectively.
Validation	Binding between the two nanobodies with MPC were validated through pull-down assay and gel filtration. Effects of the nonobodies on MPC transport activity were examined by pyruvate transport assay.

Eukaryotic cell lines

Policy information about cell lines and Sex and Gender in Research

Cell line source(s)	Expi293F cell line was from Thermo Fisher Scientific.
Authentication	No further authentication was performed for commercially available cell line.
Mycoplasma contamination	The cell line was tested negative for mycoplasma contamination.
Commonly misidentified lines (See ICLAC register)	No commonly misidentified cell lines were used.